

The Glow of Axion Quark Nugget Dark Matter: (I) Large Scale Structures

Fereshteh Majidi,^a Xunyu Liang,^a Ludovic Van Waerbeke,^a Ariel Zhitnitsky,^a Michael Sekatchev,^a Julian S. Sommer,^b Klaus Dolag,^{b,c} Tiago Castro^d

^aDepartment of Physics and Astronomy,
University of British Columbia,
V6T 1Z1 Vancouver, BC, Canada

^bUniversitäts-Sternwarte, Fakultät für Physik,
Ludwig-Maximilians Universität,
Scheinerstr. 1,
81679 München, Germany,

^cMax-Planck-Institut für Astrophysik,
Karl-Schwarzschild-Straße 1,
85741 Garching, Germany

^dOsservatorio Astronomico di Trieste, Villa Bazzoni
Via Bazzoni, 2, 34143 Trieste TS, Italy

E-mail: fereshtehmajidi@phas.ubc.ca

Abstract. Axion quark nuggets (AQN) are hypothetical, macroscopically large objects with a mass greater than a few grams and sub-micrometer size, formed during the quark-hadron transition. Originating from the axion field, they offer a possible resolution of the similarity between visible and dark components of the Universe, i.e. $\Omega_{\text{DM}} \sim \Omega_{\text{visible}}$ and observed matter-antimatter asymmetry. These composite objects behave as cold dark matter, interacting with ordinary matter and resulting in pervasive electromagnetic radiation throughout the Universe. This work aims to predict the electromagnetic signature in large-scale structures from this AQN-baryon interaction, accounting for thermal and non-thermal radiations.

We use *Magneticum* hydrodynamical simulations to describe the realistic distribution and dynamics of gas and dark matter at cosmological scales. We construct a light cone encompassing a 1.4 square degree area on the sky, extending up to redshift $z = 5.4$, and we calculate the electromagnetic signature across a wide range of frequencies from radio, starting at $\nu \sim 1$ GHz, up to a few keV X-ray energies. We find that the AQNs electromagnetic signature is characterized by global (monopole) and fluctuation signals. The amplitude of both signals strongly depends on the average nugget mass and the ionization level of the baryonic environment, allowing us to identify a most optimistic scenario and a minimal configuration. The signal of our most optimistic scenario is often near the sensitivity limit of existing instruments, such as FIRAS in the $\nu = [100 - 500]$ GHz range and the South Pole Telescope for high-resolution $\ell > 4000$ at $\nu = 95$ GHz. Fluctuations in the Extra-galactic Background Light caused by the axion quark nuggets in the most optimistic scenario can also be tested with space-based imagers Euclid and James Webb Space Telescope. In general, our minimal configuration is still out of reach of existing instruments, but future experiments might be able to pose some constraints.

We conclude that the axion quark nuggets model represents a viable model for dark matter, which does not violate the canons of cosmology nor existing observations. A reanalysis of existing data sets could provide some evidence of axion quark nuggets if our most optimistic configuration is correct. The best chances for testing the model reside in 1) ultra-deep infrared and optical surveys, 2) future experiments to probe the frequency spectrum of the cosmic microwave background, and 3) low-frequency ($1 \text{ GHz} < \nu < 100 \text{ GHz}$) and high-resolution ($\ell \gtrsim 10^4$) observations.

Contents

1	Introduction	1
2	The Axion Quark Nugget model	3
2.1	The quark-hadron transition and the AQN formation	3
2.2	Stability of AQNs	3
2.3	Survival of AQNs and mass function	4
3	The Emission Mechanism	5
3.1	The Energy Budget	5
3.2	The Thermal Emission	6
3.2.1	Radiated Power	6
3.2.2	Effective cross-section σ_{eff}	7
3.2.3	Cooling time	9
3.2.4	Calculation of the AQN temperature T_{AQN}	10
3.2.5	The Electrosphere Spectral Emissivity	11
3.3	The Non-Thermal Emission	13
4	Simulations	14
4.1	Data cubes	15
4.2	Calculation of the specific intensity I_{ν}	16
5	Results	21
5.1	Monopole	22
5.2	Anisotropies	24
6	Discussion	25
6.1	Key results	26
6.2	Future work towards a possible detection	27
6.3	Future work: theory	28
6.4	Concluding remarks	29
A	Natural and C.G.S. units conversion	29

1 Introduction

The universe appears to be well described by a six-parameter model [1]. The composition of matter has been precisely quantified, with 75% attributed to Cold Dark Matter and 25% to baryons. Despite this success, the physical nature of dark matter (DM) remains elusive. The challenge in identifying DM arises because the possible candidates span an immense range—90 orders of magnitude in mass and cross-section, from ultra-light bosons to primordial black holes that can weigh up to 10 solar masses [2]. This vast diversity makes the comprehensive probing of the parameter space unfeasible.

From a cosmological viewpoint, there is a fundamental difference between dark matter and ordinary matter. Ordinary matter structures started to grow after the matter-radiation decoupling, while dark matter, which is pressureless, started to form gravitational structures earlier, at the matter-radiation equality. Dark matter played a key role in structure formation by giving a head start to

the gravitational collapse. The key parameter describing dark matter as a pressureless fluid is the cross-section σ to mass M_{DM} ratio, which must be sufficiently small:

$$\frac{\sigma_{\text{DM-bar}}}{M_{\text{DM}}} \ll 1 \text{ cm}^2 \text{ g}^{-1}. \quad (1.1)$$

The observational constraints on the DM-baryon scattering are from Big Bang nucleosynthesis [3, 4], spectral distortion of the Cosmic Microwave Background (CMB) [5, 6], the temperature and polarization anisotropies of the CMB [7–15], the thermal history of the intergalactic medium [16–18], the Lyman- α forest [8, 9, 13, 19], Milky Way satellite galaxies [20–22]¹, and the gas heating in galaxies [23–26] and galaxy clusters [27–29]. Generally, the constraints suggest $\sigma_{\text{DM-bar}}/M_{\text{DM}} \lesssim 10^{-3} - 0.1 \text{ cm}^2 \text{ g}^{-1}$ for the elastic DM-baryon scattering. However, the specific value greatly depends on the characteristics of the dark matter candidate. These are not very strong constraints compared to the cross-section for Weakly Interacting Massive Particles (WIMPs) $\sigma_{\text{WIMP-bar}}/M_{\text{WIMP}} \lesssim 3.4 \times 10^{-25} \text{ cm}^2 \text{ g}^{-1}$ for a typical mass $M_{\text{WIMP}} \in (10, 10^3) \text{ GeV}$ from recent direct detection [30–32]. For light DM of mass in the range of $(10^{-4}, 0.1) \text{ GeV}$, the cross section above $\sim 10^{-30} \text{ cm}^2$ is excluded by local observation and neutron stars [4, 33–35]. For even lighter particles such as axions, the axion-nucleon cross section is less than $\sim 10^{-44} \text{ cm}^2$ from neutron stars and supernova 1987A; see e.g. recent studies [36–38] and references therein. If DM is a new elementary particle, it has to be lighter than a few hundred TeV due to the unitarity limits [39]. Consequently, the cross-section must be very small to fulfill the condition (1.1). Detailed information on cosmological constraints, direct detection, and properties of DM can be found in the recent review [40].

In the present work we consider a fundamentally different type of DM where the condition (1.1) is satisfied with a large dark matter-baryon cross-section and dark matter is made of macroscopically large objects, with a mass $M_{\text{DM}} \gtrsim 1 \text{ g}$ and size of sub-micrometers. We consider a specific generalization of the Witten’s quark nuggets [41–43], the so-called axion quark nuggets (AQNs) [44]. Unlike conventional dark matter candidates such as WIMPs and axions (e.g. review [45] and references therein), AQNs interact strongly with baryonic matter. The reason is that AQNs form during the quark-hadron transition, when matter and antimatter have not yet annihilated, therefore some AQNs are made of antimatter which leads to broad bandwidth, from radio to X-ray, electromagnetic radiation when AQNs collide with normal matter.

Motivated by the unique emission properties of AQNs, we investigate the AQN signature from large-scale structures from the present-day up to redshift $z = 5.34$ using the *Magneticum* hydro simulations. We make predictions for a wide bandwidth range, from radio, where the CMB dominates, to infrared, optical and X-ray and investigate both the global (monopole) intensity and anisotropies. In general, we find that the AQN signal takes the form of radiation excess or anomalies, correlated with large scale structures. We discuss the potential detectability of the signal with existing and future observatories.

The paper is structured as follows: In section 2 we briefly review the AQN formation mechanism. In section 3 we describe the AQN emission mechanisms and the role of the baryonic environment. In section 4.1 we describe the simulations used in this work and section 4.2 shows how the light cone is constructed and how the AQN signal is calculated from the simulation. We will discuss the results in section 5, and in section 6, after summarizing our main results, we discuss possible future work, including a description of existing data that could yield a detection and long term theoretical developments.

¹For Ref. [20], there is an erratum [Astrophys. J. Lett. 897, L46 (2020)]

2 The Axion Quark Nugget model

The model was initially proposed by [44] as an explanation for why the dark matter (DM) mass density and the visible matter mass density are of the same order of magnitude, denoted as $\Omega_{\text{DM}} \sim \Omega_{\text{visible}}$. The Axion Quark Nugget (AQN) construction shares many similarities with Witten’s quark nuggets, as referenced in [41]. This form of DM is "cosmologically dark," meaning that its interaction cross-section to mass ratio, σ/m_{DM} , is significantly less than $1 \text{ cm}^2\text{g}^{-1}$. This numerically small ratio reduces many electromagnetic signatures that would typically be associated with a strongly-interacting DM candidate, thereby ensuring that AQN kinematics align with those of cold dark matter (CDM), which is pressureless. In the subsequent sections, we will briefly review the primary steps involved in the formation of an AQN. For more detailed information, interested readers are referred to a recent concise review [46].

2.1 The quark-hadron transition and the AQN formation

The formation of AQNs is dependent on the so-called $N = 1$ QCD axion domain wall bubbles, as detailed in references [47–50]. It is generally assumed that these closed domain wall bubbles are abundantly produced and collapse without leaving observable traces. Within the AQN model, however, some of these bubbles manage to persist by accreting quarks, thereby forming AQNs in which the internal Fermi pressure counterbalances the external wall pressure. The accretion process becomes particularly effective during the quark-hadron transition when the temperature of the universe reaches approximately $\sim 170 \text{ MeV}^2$. The quarks confined within these bubbles then exhibit a pronounced matter-antimatter asymmetry due to the charge separation, a characteristic effect of the $C\mathcal{P}$ -odd axion field’s interaction with matter and antimatter. As matter-antimatter annihilation persists in the plasma, both matter and antimatter nuggets form in proportions comparable to that of the newly created hadronic matter (protons and neutrons) outside the closed bubbles.

As the system continues to cool down, baryons and anti-baryons outside the bubbles persist in annihilating each other until all anti-baryons are depleted. The nuggets formed during the QCD transition may consist of both *matter* and *antimatter* AQNs. A significant implication of this characteristic—considering the Universe’s total baryon charge is zero—is that the densities of dark matter (DM), Ω_{DM} (represented in this context by both matter and antimatter nuggets), and visible baryonic matter, Ω_{visible} , will naturally align to the same order of magnitude, $\Omega_{\text{DM}} \sim \Omega_{\text{visible}}$. This correlation occurs independently of specific model details, such as the axion mass m_a ³.

2.2 Stability of AQNs

The interior of nuggets is composed of matter in the form of a diquark condensate, which exists in the color superconducting phase. This phase is recognized as the lowest energy state under sufficiently high pressures and may be present in the cores of neutron stars (NS), as discussed in the review [51]. A practical approach to understanding nuggets is to consider them analogous to miniature NS, hold together by the axion domain wall tension, with masses ranging from a gram to several tons. Importantly, the energy per baryon charge in the quark-matter nuggets is lower than in hadrons, indicating that AQNs are more stable than protons and neutrons.

There are several additional elements in the AQN model in comparison with the older constructions of the Witten’s nuggets [41–43]. Firstly, AQNs can be made of *matter* as well as *antimatter* during the QCD transition as we already mentioned. Secondly, there is an additional stabilization

²This energy scale corresponds to the Quantum Chromo Dynamic (QCD) energy scale.

³An exact calculation of the mass densities would require a full solution to the strongly coupled QCD problem, which is currently unachievable.

Table 1. Mass m_{AQN} and radius R_{AQN} of an AQN using the nuclear mass density $\rho_{\text{nuc}} = 3.5 \times 10^{14} \text{ g cm}^{-3}$ [52] for the quark-gluon material. To calculate the number density n_{AQN} , we use a dark matter mass density $\rho_{\text{DM}} = 0.3 \text{ GeV m}^{-3}$, which corresponds to the average cosmological DM mass density today ($z = 0$) for a $\Omega_{\text{DM}} = 0.266$ universe, and assuming that all dark matter is made of AQNs. The number density is $n_{\text{AQN}} = \frac{2}{3} \times \frac{3}{5} \frac{\rho_{\text{DM}}}{m_{\text{AQN}}}$, which considers only the antimatter AQNs with axion contribution excluded.

m_{AQN} [g]	R_{AQN} [cm]	n_{AQN} [m^{-3}]
1	8.8×10^{-6}	9.0×10^{-25}
10	1.9×10^{-5}	9.0×10^{-26}
100	4.1×10^{-5}	9.0×10^{-27}
1000	8.8×10^{-5}	9.0×10^{-28}

factor for the nuggets provided by the axion domain walls which are copiously produced during the QCD transition. This additional element helps to alleviate a number of problems with the Witten’s original model. In particular, a first-order phase transition (which is now known to not occur in QCD) was a required feature for the Witten’s nuggets to be formed. It is not required for AQN formation because the axion domain wall (with internal QCD substructure) plays the role of the squeezer, keeping the quark (anti-quark) matter stable. Another problem of the old construction [41–43] is that nuggets likely evaporate on the Hubble timescale. For the AQN model, this is not the case because the vacuum-ground-state energies inside (the colour- superconducting phase) and outside the nugget (the hadronic phase) are drastically different. Therefore, these two systems can coexist only in the presence of an external pressure, provided by the axion domain wall, which is an inevitable feature of the AQN construction. This should be contrasted with the original model [41–43], which is assumed to be stable at zero external pressure. These differences have important phenomenological implications: In Witten’s model, the nuggets were postulated to be stable even at zero external pressure, as mentioned above. In scenarios where they collide with a neutron star, the model suggests that the entire neutron star would be converted into a quark star. In the AQN model a matter-type AQN will not transform an entire neutron star into a quark star. This is because the quark matter within AQNs is maintained by the pressure from external axion domain walls, limiting its expansion to only a small region rather than the entire star.

2.3 Survival of AQNs and mass function

The mass m_{AQN} of an AQN is the only fundamental parameter of the model, though it is relatively insensitive to the fundamental mass of the axion field m_a . For a given m_a , the AQN size cannot exceed $R_{\text{AQN}}^{\text{max}} \sim m_a^{-1}$ [47]. Therefore, the AQN mass follows a distribution with a high mass cutoff constrained by the axion mass m_a which can only be determined experimentally. Various observational limits on Macroscopic Dark Matter size imposes a constraint on their number density, which, in the context of the AQN model, allows the nugget mass to be anywhere between 1 g and higher. According to [53], the most stringent constraint on $\langle m_{\text{AQN}} \rangle$ is greater than 5 grams, derived from the lack of detection at the IceCube observatory. Similar constraints are reported by the ANITA experiment and from geothermal data [54]. While the exact mass distribution function of AQNs remains unknown, percolation simulations suggest that it follows a power-law distribution [50].

Table 1 presents the sizes and number densities of AQNs for various masses. Given their nuclear density, these objects are extremely compact, and their substantial mass, relative to typical particle physics standards, results in a notably low number density⁴. It is sometimes beneficial to utilize the

⁴For comparison, the average number density of WIMPs in the universe today is approximately $n_{\text{WIMP}} \approx 10^{-3} \text{ m}^{-3}$ for

baryon charge B (equivalent to the proton mass) as a proxy for mass [53]:

$$B \gtrsim 3 \times 10^{24} . \quad (2.1)$$

The AQN mass, geometrical cross-section σ_{geo} and number density can be written as [46]:

$$\begin{aligned} m_{\text{AQN}} &\approx 16.7 \left(\frac{B}{10^{25}} \right) \text{ g} \\ \sigma_{\text{geo}} &\equiv \pi R_{\text{AQN}}^2 \approx 1.59 \times 10^{-9} \left(\frac{R_{\text{AQN}}}{2.25 \times 10^{-5} \text{ cm}} \right)^2 \text{ cm}^2 \\ n_{\text{AQN}} &\equiv \frac{\rho_{\text{DM}}}{m_{\text{AQN}}} \sim 0.3 \times 10^{-25} \left(\frac{10^{25}}{B} \right) \text{ cm}^{-3} \end{aligned} \quad (2.2)$$

where we have used $\rho_{\text{DM}} = 0.3 \text{ GeV cm}^{-3}$. Antimatter AQNs experience mass loss, denoted as ΔB , even after their formation, primarily due to interactions and subsequent annihilations with baryons. It has been calculated that the ratio $\Delta B/B \ll 1$ remains consistent across all cosmic epochs, including during the Big Bang Nucleosynthesis, as well as the pre- and post-recombination and galaxy formation periods [50, 55–57]. This finding is further corroborated by independent analyses from [58] and [59].

For the remainder of this paper, our focus will be on the electromagnetic signatures of antimatter nuggets. We will consider a fixed nugget mass m_{AQN} , with consistent nuclear density and radius, denoted as n_{AQN} and R_{AQN} , respectively. Although our calculations can be extended to account for a mass distribution, we opt for fixed values for simplicity. The relaxing of this constraint will make the allowed window for B broader.

3 The Emission Mechanism

3.1 The Energy Budget

In the AQN model, matter-based AQNs are surrounded by a cloud of electrons, while antimatter AQNs are surrounded by a cloud of positrons, both configurations serving to maintain electrical neutrality. For the purposes of this paper, the cloud surrounding antimatter AQNs will be referred to as the electrosphere. When a matter AQN collides with conventional matter, the energy exchange is minimal, leading to negligible radiation. Conversely, collisions between antimatter AQNs and regular matter (such as protons, hydrogen, and helium) results in annihilation events that release substantial amounts of energy. Within the AQN framework, the absence of an electromagnetic signature from dark matter is not due to exceedingly weak interactions with baryons⁵, but it is instead attributed to the significantly lower number density of AQNs compared to baryons ($n_{\text{AQN}} \ll n_{\text{b}}$), despite the strong interaction between antimatter AQNs and baryons⁶.

The collision rate of an AQN with the surrounding baryonic matter is given by:

$$\Gamma = \sigma_{\text{eff}} n_{\text{b}} \Delta v , \quad (3.1)$$

where σ_{eff} is the effective cross-section of the AQN, n_{b} is the baryon number density, and $\Delta v = |\vec{v}_{\text{AQN}} - \vec{v}_{\text{b}}|$ is the relative speed between an AQN and a baryon. The effective cross-section σ_{eff}

a WIMP mass of 100 – 200 GeV, which is at least 20 orders of magnitude greater than n_{AQN}

⁵as it should be the case for WIMPs.

⁶Note that "strong interaction" refers to the large dark matter-baryon interaction cross-section, not to the strong nuclear force.

describes the area around the AQN capable of capturing baryonic matter, potentially triggering an annihilation event. σ_{eff} is not necessarily equal to the geometrical cross-section σ_{geo} . This is the case when the AQN acquires a non-zero electrical charge and the baryonic environment is ionized, and the Coulomb force could significantly change the cross-section. The calculation of σ_{eff} under this condition will be explored in Section 3.2.2.

Nuggets predominantly collide with atomic or ionized hydrogen and helium, the most abundant elements in the universe. For each collision, the incoming baryonic matter will either rebound due to quantum reflection [60] or be captured, penetrate the nugget's core, and annihilate. The likelihood of quantum reflection has a probability $(1 - f)$. The specific value of f depends on the model, but assuming $1 - f \sim 0.9$ is considered reasonable [60]. For matter that penetrates the core, the energy available for photon production from the annihilation is twice the rest mass of the incoming particle⁷, and the kinetic energy is negligible. A fraction g of this energy will be emitted as a short pulse of non-thermal photons at the point of impact, while a remaining fraction $(1 - g)$ will be transferred as heat into the AQN anti-quarks core and subsequently to the electrosphere which will emit thermally⁸. As will be discussed in Section 3.2.3, the substantial heat capacity of the anti-quark matter results in a cooling time significantly longer than the average time between collisions. Consequently, the AQN reaches thermal equilibrium at some temperature T_{AQN} , and the electrosphere emits thermally. Meanwhile, the energy released at the point of impact can escape the system immediately via non-thermal processes.

For simplicity, we will assume that the incoming particle is a proton, thus corresponding to 2 GeV of energy. The energy $\Delta E_{\text{ann}}^{\text{th}}$ emitted thermally is therefore given by:

$$\Delta E_{\text{ann}}^{\text{th}} = 2 \text{ GeV} f (1 - g), \quad (3.2)$$

which corresponds to the power:

$$\frac{dE_{\text{ann}}^{\text{th}}}{dt} = \Delta E_{\text{ann}}^{\text{th}} \Gamma = 2 \text{ GeV} f (1 - g) \sigma_{\text{eff}} n_{\text{b}} \Delta v. \quad (3.3)$$

The non-thermal photons will be radiated away in a short pulse during the annihilation event, delivering an average power (per event):

$$\frac{dE_{\text{ann}}^{\text{non-th}}}{dt} = 2 \text{ GeV} f g \sigma_{\text{eff}} n_{\text{b}} \Delta v. \quad (3.4)$$

Therefore, any annihilation event will produce two outcomes: 1- it sustains the electrosphere at an equilibrium temperature T_{AQN} , which consequently emits thermal radiation continuously, and 2- it generates a pulse of non-thermal photons at the point of impact.

3.2 The Thermal Emission

3.2.1 Radiated Power

We now focus on the electromagnetic radiation emitted from the heated electrosphere. The primary factor influencing photon emissivity in this scenario is the nugget temperature, T_{AQN} . As discussed

⁷Strictly speaking, axions contribute a significant fraction of the radiation, approximately 1/3 of the total [49]. We adjust for the axion contribution by defining the number density:

$$n_{\text{AQN}} = \frac{2}{3} \times \frac{3}{5} \frac{\rho_{\text{DM}}}{m_{\text{AQN}}},$$

where 2/3 is the non-axion fraction of a nugget mass, 3/5 is the fraction of antimatter nuggets as explained in the preceding subsection.

⁸Similar to f , the factor g is also highly model dependent and must be less than unity. We use $g \simeq 0.1$, as discussed in [61]. A small fraction of the annihilation energy will convert to subatomic particles, which we are neglecting.

in Section 3.1, T_{AQN} is determined by the annihilation rate within the nugget, which itself depends on the surrounding baryonic environment (whether it is ionized or not) and the collision rate.

When the anti-quark core of the nugget is at zero temperature ($T_{\text{AQN}} = 0$), all positrons occupy Fermi levels beneath the surface of the nugget, meaning that they behave similarly to degenerate electrons in a white dwarf. Owing to the Pauli exclusion principle, positrons in this state cannot change their quantum states, and thus, no radiation is produced. However, at non-zero temperatures, a thin layer of positrons forms above the core, occupying Boltzmann states, which enables photon emission. As shown in [62], positrons near the core are relativistic, while those further from the core are not, with the latter emitting thermal photons through Bremsstrahlung [60, 61]. The flux density emitted by a single nugget, $F_{\text{tot}}^{\text{th}}(T_{\text{AQN}})$, is derived in [61]:

$$F_{\text{tot}}^{\text{th}}(T_{\text{AQN}}) = \frac{16\alpha^{5/2}}{3\pi} T_{\text{AQN}}^4 \left(\frac{T_{\text{AQN}}}{m_e} \right)^{1/4}, \quad (3.5)$$

where α is the fine structure constant, and m_e the electron mass. In this work, we have adopted natural units, setting \hbar , k_B , and c to 1. The total power emitted by the electrosphere is isotropic and can be formulated as ⁹:

$$\frac{dE_{\text{ann}}^{\text{th}}}{dt} = 4\pi R_{\text{AQN}}^2 F_{\text{tot}}^{\text{th}}(T_{\text{AQN}}). \quad (3.6)$$

It is important to note that Eq. (3.5) and (3.6) are only valid if the AQN is in thermal equilibrium. The equilibrium temperature of the electrosphere, T_{AQN} , is determined by the annihilation rate inside the core, which in turn depends on the effective cross-section σ_{eff} , as indicated by Eq. (3.1), and on the cooling time. In the following section, we will calculate σ_{eff} , and in Section 3.2.3, we will determine the cooling time. A cooling time that exceeds the collision time is necessary to maintain the thermal equilibrium of the AQN electrosphere.

3.2.2 Effective cross-section σ_{eff}

To calculate σ_{eff} , it is essential to consider that the AQN may acquire a net negative electrical charge Q at non-zero temperatures. This occurs because, when $T_{\text{AQN}} > 0$, the least bound positrons can escape the system, leading to $Q < 0$. This will increase σ_{eff} when the surrounding baryonic environment contains positively charged ions.

The charge Q is calculated under the assumption that positrons with kinetic energy exceeding the potential energy will escape. This relationship is formalized as follows [63]:

$$|Q| \simeq 4\pi R_{\text{AQN}}^2 \int_0^\infty n(z, T_{\text{AQN}}) dz = \frac{4\pi R_{\text{AQN}}^2}{\sqrt{2\pi\alpha}} (m_e T_{\text{AQN}}) \left(\frac{T_{\text{AQN}}}{m_e} \right)^{1/4}. \quad (3.7)$$

Here, $n(z, T_{\text{AQN}})$ represents the local density of positrons at a distance z from the nugget's surface, calculated using the mean field approximation [61]:

$$n(z, T_{\text{AQN}}) = \frac{T_{\text{AQN}}}{2\pi\alpha} \frac{1}{(z + \bar{z})^2}. \quad (3.8)$$

In this equation, \bar{z} is an integration constant determined numerically to align with the Boltzmann regime.

⁹In C.G.S. physical units, the quantity F_{tot} is measured in $\text{erg s}^{-1}\text{cm}^{-2}$. While we use natural units in the main text to streamline discussions involving orders of magnitude. For those accustomed to the C.G.S. system, refer to Table 4 in Appendix A.

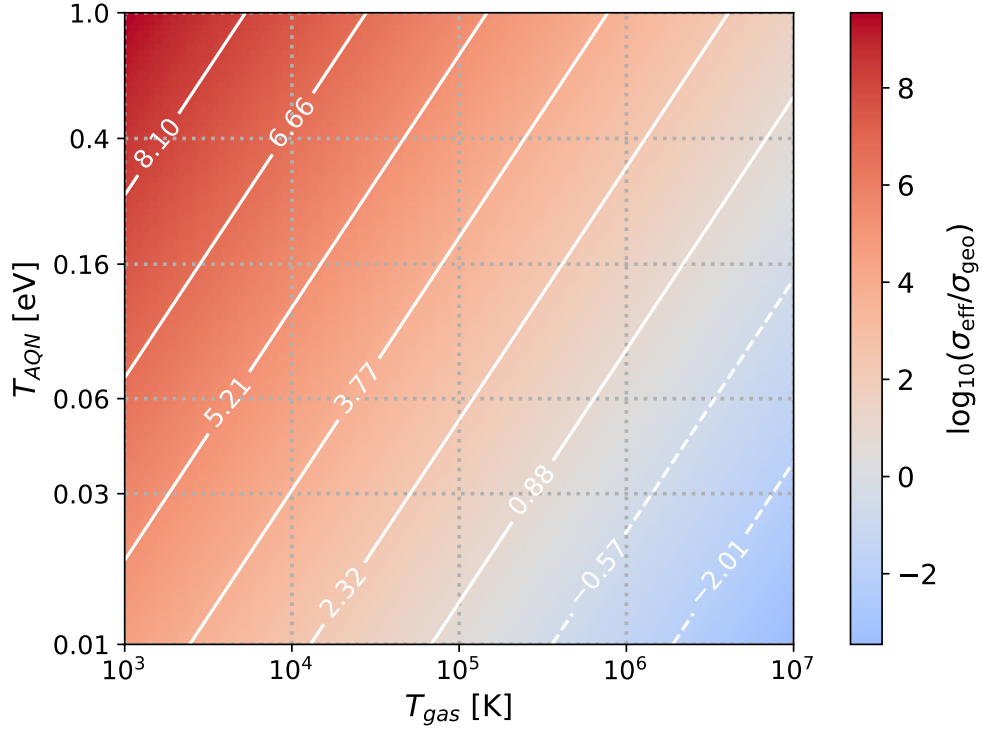


Figure 1. Cross-section ratio $\sigma_{\text{eff}}/\sigma_{\text{geo}}$ given by Eq. (3.11) for an AQN mass $m_{\text{AQN}} = 10$ g and with $\Delta v = 10^{-3}c$. The gradian shows how the effective cross-section σ_{eff} compares to the geometrical cross-section σ_{geo} when the baryons temperature T_{gas} of the environment around the AQN varies for a given AQN temperature T_{AQN} . It is expected that in real physical environments, one has to set $\sigma_{\text{eff}} = \sigma_{\text{geo}}$ in the bottom-right region of the plot and when the baryon gas is no longer ionized (see conditions 1 and 2 respectively in Section 3.2.2).

$$\bar{z}^{-1} \simeq \sqrt{2\pi\alpha} m_e \left(\frac{T_{\text{AQN}}}{m_e} \right)^{1/4}. \quad (3.9)$$

When $Q < 0$, the AQN will capture surrounding free protons (or any positively charged ionized nuclei) with an effective impact parameter R_{eff} larger than the AQN radius R_{AQN} . The equality between the kinetic energy and the Coulomb potential energy is used to define R_{eff} :

$$\frac{\alpha Q}{R_{\text{eff}}} \sim T_{\text{gas}}, \quad (3.10)$$

where T_{gas} denotes the temperature of the surrounding ionized gas. The interpretation of Eq. (3.10) is straightforward: with a constant charge Q , a lower T_{gas} leads to charged particles being more easily deflected by the Coulomb potential of the AQN, thus increasing the effective radius, R_{eff} . Conversely, a higher T_{gas} reduces R_{eff} .

Combining Eqs. (3.7) and (3.10) and defining $\sigma_{\text{eff}} = \pi R_{\text{eff}}^2$, we obtain:

$$\frac{\sigma_{\text{eff}}}{\sigma_{\text{geo}}} = \left(\frac{R_{\text{eff}}}{R_{\text{AQN}}} \right)^2 = 8\alpha m_e^2 R_{\text{AQN}}^2 \left(\frac{T_{\text{AQN}}}{T_{\text{gas}}} \right)^2 \sqrt{\frac{T_{\text{AQN}}}{m_e}}. \quad (3.11)$$

It is very important, for the rest of this paper, to emphasize that there are two limiting cases where Eq. (3.11) should not be used:

Condition 1- When T_{gas} is high enough to result in $R_{\text{eff}} < R_{\text{AQN}}$, the baryons in the AQN rest frame move so rapidly that their capture becomes unlikely, and the cross-section effectively reduces to the geometrical cross-section, i.e. head-on collisions¹⁰.

Condition 2- When the surrounding gas is not ionized. This typically occurs when T_{gas} falls below a certain threshold. However, in general, the specific conditions for non-ionized gas depend on the particular astrophysical environment, and a simple temperature threshold is not a sufficient criterion for deciding when the gas is ionized or not.

If either condition 1 or 2 applies, the geometrical cross-section should be used, i.e., $\sigma_{\text{eff}} = \sigma_{\text{geo}}$. It is crucial to recognize that when neither of these conditions is met, the quantum reflection probability $1 - f$, as defined in Section 3, effectively becomes zero. This occurs because, once captured, the baryon is certain to annihilate with the AQN anti-quark matter ($f = 1$), although with a time delay that is irrelevant for our purpose.

Using Eq. (3.11), $\sigma_{\text{eff}}/\sigma_{\text{geo}}$ is shown in Figure 1 as a function of T_{gas} and T_{AQN} for an AQN with a mass of $m_{\text{AQN}} = 10g^{\text{u}}$. The bottom-right corner of Figure 1, where $\sigma_{\text{eff}} < \sigma_{\text{geo}}$, indicates where condition 1 is applicable. Conversely, on the left side of the figure, where T_{gas} is lower, the baryonic matter is likely to have recombined into neutral atomic form, necessitating the application of condition 2. Hence, the specific conditions under which condition 2 applies are heavily dependent on the astrophysical environment, such as the baryon number density and the expansion rate of the universe. When either condition 1 or 2 is applicable, $\sigma_{\text{eff}} = \sigma_{\text{geo}}$ must be used.

3.2.3 Cooling time

We now possess all the essential equations required to calculate the AQN temperature; however, the thermal equilibrium condition, crucial for applying Eq. (3.5), must be validated. The thermal equilibrium can be established and maintained only if the AQN cooling time, t_{cool} , exceeds the mean collision time, $t_{\text{coll}} \sim \Gamma^{-1}$, as specified in Eq. (3.1). Using the previous equations and assumptions, we now demonstrate that the framework consistently supports $t_{\text{cool}} \gg t_{\text{coll}}$.

The cooling time is calculated by solving Eq. (17) from [64]:

$$\frac{dT_{\text{AQN}}(t)}{dt} = -\frac{3F_{\text{tot}}^{\text{th}}(T_{\text{AQN}})}{R_{\text{AQN}} c_v(T_{\text{AQN}})}. \quad (3.12)$$

Here, c_v represents the specific heat of the core material, defined as:

$$c_v \simeq \frac{1}{3}T_{\text{AQN}}(\mu_d^2 + \mu_u^2). \quad (3.13)$$

In this formula, the chemical potentials μ_d and μ_u , each approximately 500 MeV, correspond to the nuclear material in the color superconducting phase. Solving Eq. (3.12) determines the cooling time scale, t_{cool} :

$$t_{\text{cool}} = \frac{\pi\mu_{u,d}^2 R_{\text{AQN}} m_e^{1/4}}{54\alpha^{5/2} T_0^{9/4}}. \quad (3.14)$$

Here, T_0 represents an arbitrary initial temperature of the AQN at $t = 0$. Within a cosmological context, the typical range of AQN temperatures is $T_{\text{AQN}} \in [10^{-2}, 1]\text{eV}$. Calculations of t_{cool} with

¹⁰Note that the only situation in which $R_{\text{eff}} < R_{\text{AQN}}$ physically occurs is when the baryonic matter is negatively charged, a possibility not considered in this work.

¹¹The range of $T_{\text{gas}} \sim 10^3 - 10^4\text{K}$ typically corresponds to cosmic voids, while a T_{gas} exceeding 10^6K characterizes galaxy clusters.

T_0 in this range yield cooling times between 10^{12} s and 10^8 s, which is approximately four orders of magnitude larger than the average time between two collisions, Γ^{-1} . Hence, we conclude that the AQN positron sphere consistently remains in thermal equilibrium, verifying that Eq. (3.5) is an excellent approximation for the considered range of n_b and T_{gas} .

3.2.4 Calculation of the AQN temperature T_{AQN}

The electrosphere temperature, T_{AQN} , can be calculated by combining Eqs. (3.3) and (3.6) and using Eq. (3.11) for σ_{eff} . The resulting T_{AQN} , when neither conditions 1 nor 2 apply, is given by:

$$T_{\text{AQN}}|_{\text{eff}} = m_e \left[\frac{2\text{GeV} f(1-g)}{8\alpha^{3/2} T_{\text{gas}}^2} 3\pi n_b \Delta v R_{\text{AQN}}^2 \right]^{\frac{4}{7}}. \quad (3.15)$$

Note that it is typically appropriate to set $f = 1$ (since all captured charged particles will eventually annihilate), but we retain f in the formula for clarity. Additionally, we use the subscript *eff* to signify that this expression is valid only when Eq. (3.11) holds. This equation can also be expressed as a product of dimensionless ratios, as detailed in Table 4 in Appendix A:

$$T_{\text{AQN}}|_{\text{eff}} = 1.4 \times 10^3 \text{ eV} \left(\frac{n_b}{1 \text{ cm}^{-3}} \right)^{\frac{4}{7}} \left(\frac{\Delta v}{10^{-3} c} \right)^{\frac{4}{7}} \left(\frac{f(1-g)}{0.9} \right)^{\frac{4}{7}} \times \left(\frac{R_{\text{AQN}}}{2.25 \times 10^{-5} \text{ cm}^{-3}} \right)^{\frac{8}{7}} \left(\frac{1 \text{ eV}}{T_{\text{gas}}} \right)^{\frac{8}{7}}. \quad (3.16)$$

When conditions 1 or 2 apply, Eq. (3.11) does not hold anymore, and we must use $\sigma_{\text{eff}} = \sigma_{\text{geo}}$, the AQN temperature is then given by:

$$T_{\text{AQN}}|_{\text{geo}} = \left[\frac{3\pi}{4} \frac{2 \text{ GeV}}{16\alpha^{5/2}} f(1-g) m_e^{1/4} \Delta v n_b \right]^{4/17}. \quad (3.17)$$

The subscript *geo* indicates that Eq. (3.17) specifically pertains to the geometrical cross-section.

Note that it is possible to combine Eqs. (3.15) and (3.17) into a single expression for T_{AQN} which works for both the effective and geometrical cases, if the right hand side is expressed as a function of $\sigma_{\text{eff}}/\sigma_{\text{geo}}$:

$$T_{\text{AQN}} = \left[\frac{3\pi}{4} \frac{2 \text{ GeV}}{16\alpha^{5/2}} f(1-g) m_e^{1/4} \Delta v n_b \left(\frac{\sigma_{\text{eff}}}{\sigma_{\text{geo}}} \right) \right]^{4/17}. \quad (3.18)$$

This equation is useful for directly calculating T_{AQN} from Eq. (3.11), as long as we use $\sigma_{\text{eff}} = \sigma_{\text{geo}}$ if either condition 1 or 2 applies. One can see that Eq. (3.18) is identical to Eq. (3.17) when $\sigma_{\text{eff}} = \sigma_{\text{geo}}$, and identical to Eq. (3.15) otherwise.

Figure 2 displays the ratio $T_{\text{AQN}}/T_{\text{gas}}$ using Eq. (3.18) as a function of T_{gas} for three different values of n_b . On this Figure, we arbitrarily choose a sharp transition from ionized to neutral atomic baryonic gas at $T_{\text{gas}} = 3 \times 10^4 \text{ K}$ for illustration purposes. Each curve is divided into three segments with varying slopes: the leftmost segment, under $T_{\text{gas}} = 3 \times 10^4 \text{ K}$, where condition 2 would apply, indicating a neutral atomic environment; a middle segment where Eq. (3.11) is applicable; and a rightmost segment at high T_{gas} where condition 1 applies. The segments under conditions 1 and 2 exhibit identical slopes.

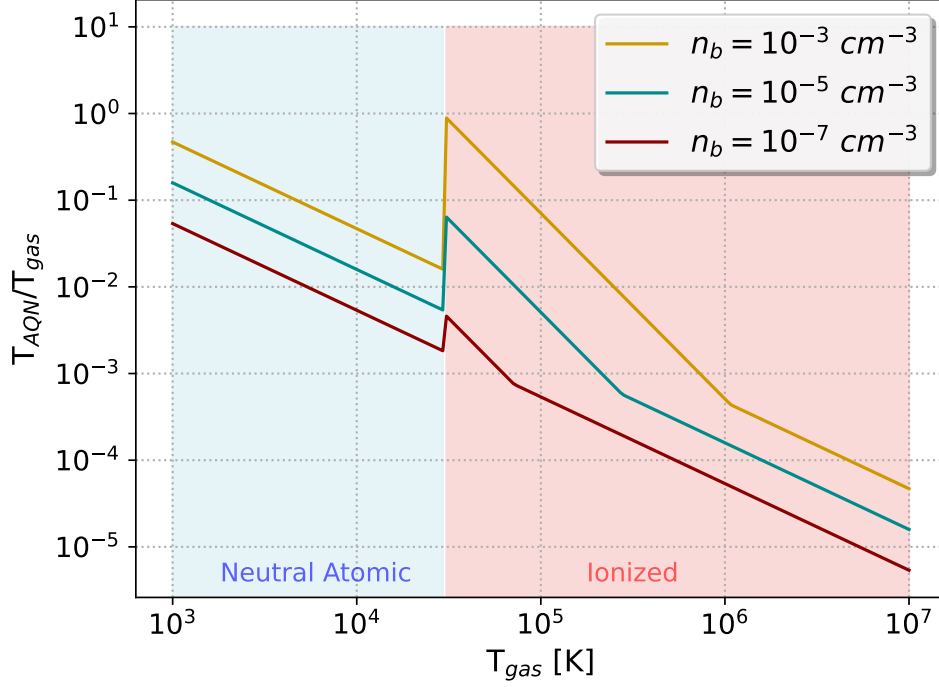


Figure 2. AQN temperature over baryon gas temperature, $T_{\text{AQN}}/T_{\text{gas}}$, as a function of T_{gas} and for different baryon number density $n_b = [10^{-3}, 10^{-5}, 10^{-7}] \text{ cm}^{-3}$ for the yellow, blue and red lines respectively. The nugget mass is $m_{\text{AQN}} = 10 \text{ g}$ and $\Delta v = 10^{-3}c$. The jump in all curves at $T_{\text{gas}} = 3 \times 10^4 \text{ K}$ corresponds to the rapid decrease of the effective cross-section σ_{eff} down to σ_{geo} when the baryonic environment is no longer ionized. The choice of $3 \times 10^4 \text{ K}$ was chosen arbitrarily and only serves for illustration purposes, its real value depends on the specific environment. Each curve also shows a high T_{gas} transition, which comes from the fact that the effective cross-section can never decrease below the geometrical cross-section.

3.2.5 The Electrosphere Spectral Emissivity

The emission spectrum $F_{\nu}^{\text{th}}(T_{\text{AQN}})$ of the electrosphere was derived in [61]:

$$F_{\nu}^{\text{th}}(T_{\text{AQN}}) = \frac{8}{45} T_{\text{AQN}}^3 \alpha^{5/2} \left(\frac{T_{\text{AQN}}}{m_e} \right)^{1/4} H \left(\frac{2\pi\nu}{T_{\text{AQN}}} \right). \quad (3.19)$$

Here, the function $H(x)$ is defined as:

$$H(x) \simeq \begin{cases} (1+x)e^{-x}(17 - 12 \ln(x/2)), & \text{if } x < 1; \\ (1+x)e^{-x}(17 + 12 \ln(2)), & \text{if } x \geq 1. \end{cases} \quad (3.20)$$

where the term $2\pi\nu$ in $H(x)$ denotes the angular frequency, expressed in natural units (see Table 3 in Appendix A)¹². The exponential dependence on frequency ν in Eq. (3.19) is characteristic of the thermal Bremsstrahlung emission. However, the low-frequency behavior deviates slightly from conventional Bremsstrahlung, influenced by the geometry and size of the positron cloud, as noted in

¹²In natural units, it is common to use the angular frequency ω , such that in C.G.S. systems, $h\nu$ is replaced by $\hbar\omega$, consistent with the use of $\hbar = 1$. However, in astrophysics, the frequency ν is typically used because it can be directly compared to the observational capabilities of radio telescopes.

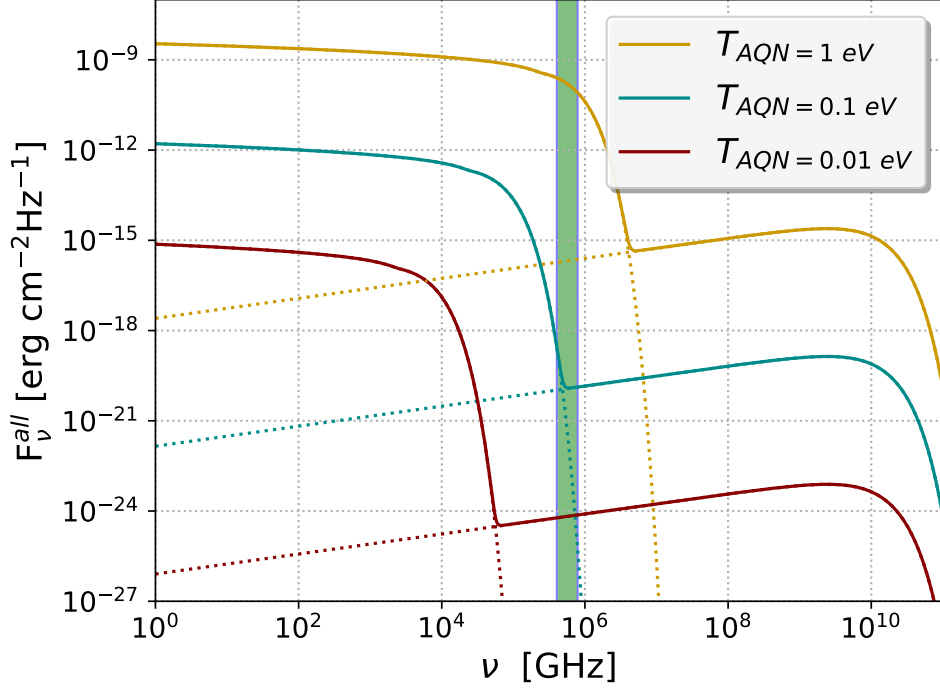


Figure 3. The solid lines show the total emission spectrum $F_\nu^{\text{all}} = F_\nu^{\text{th}} + F_\nu^{\text{non-th}}$ for AQNs at different temperatures $T_{\text{AQN}} = [1, 10^{-1}, 10^{-2}]$ eV for the yellow, blue and red lines respectively. Each solid line is the sum of thermal [Eq. (3.19)] and non-thermal [Eq. (3.29)] emissions. The dotted lines show the separation between the thermal and non-thermal components. The thermal contribution dominates at low frequency in radio, while the non-thermal contribution dominates at high frequency in X-ray. The vertical green region represents the optical range of frequencies. One can see how the emission spectrum in the optical range is highly dependent on the AQN temperature.

[61]. Below $\nu \sim 1$ GHz, Eq. (3.19) becomes invalid and more theoretical work is necessary to extend it to lower frequencies. For the purposes of this work, we will disregard this limitation as it occurs at frequencies outside our range of interest.

The C.G.S. unit for $F_\nu^{\text{th}}(T_{\text{AQN}})$ is $\text{erg s}^{-1} \text{cm}^{-2} \text{Hz}^{-1}$. For consistency, we should note that Eq. (3.5) is the integral of Eq. (3.19) over ν :

$$F_{\text{tot}}^{\text{th}}(T_{\text{AQN}}) = \int_0^\infty d\nu F_\nu^{\text{th}}(T_{\text{AQN}}). \quad (3.21)$$

Figure 3 displays $F_\nu^{\text{th}}(T_{\text{AQN}})$ for different values of T_{AQN} , along with the non-thermal emission, which will be calculated in Section 3.3. In the radio range, the amplitude of the spectrum scales approximately as $\sim T_{\text{AQN}}^{3.25}$. However, in the infrared-UV range, the amplitude is highly dependent on T_{AQN} due to the exponential factor. This characteristic is particularly interesting for designing tests of the model, which will be further discussed in the conclusion section.

In order to evaluate the radiation emanating from a spatial region containing a number density n_{AQN} of AQNs, one must compute the so-called spectral emissivity $\epsilon_\nu^{\text{th}}(T_{\text{AQN}})$ emitted from AQN-baryon collisions per unit time, volume, and frequency, which is given by:

$$\epsilon_\nu^{\text{th}}(T_{\text{AQN}}) = 4\pi R_{\text{AQN}}^2 F_\nu^{\text{th}}(T_{\text{AQN}}) n_{\text{AQN}}. \quad (3.22)$$

The C.G.S. unit for $\epsilon_\nu^{\text{th}}(T_{\text{AQN}})$ is $\text{erg s}^{-1} \text{cm}^{-3} \text{Hz}^{-1}$.

In summary, we have outlined the methodology to calculate the thermal emissivity spectrum of the AQN dark matter, once the macroscopic parameters—specifically the AQN number density n_{AQN} , the baryon number density n_b , the gas temperature T_{gas} and the relative velocity between dark matter and baryons—are known. The only fundamental free parameter¹³ of the model is the AQN mass m_{AQN} since it determines its size R_{AQN} . It is expected that the AQN mass should follow a power law distribution, but in this work we consider a fixed value of the mass for simplicity as explained in Sect.2.3.

3.3 The Non-Thermal Emission

As discussed in Section 3.1, the collision of an antimatter AQN with a baryon also results in non-thermal emission, manifesting as a short pulse of predominantly X-ray photons in the ~ 1 -10 keV range [60]. This non-thermal emission originates from the Bremsstrahlung of relativistic positrons at the impact site by the mean field of surrounding positrons. Unlike the thermal process, this emission does not first involve heat transfer through the anti-quarks core, which allows the radiation to escape immediately and results in the short duration of the pulse. For a collision with a proton, the total amount of energy per event is given by:

$$\Delta E_{\text{ann}}^{\text{non-th}} \approx 2 \text{ GeV} f g \quad (3.23)$$

The chemical potential of these positrons, located deep within the electrosphere, is approximately $\mu \sim 10 \text{ MeV}$. They emit X-rays through Bremsstrahlung, characterized by a qualitative spectrum:

$$F_\nu^{\text{non-th}} \propto \frac{\nu}{\nu_c} \int_{\nu/\nu_c}^{\infty} K_{5/3}(x) dx, \quad (3.24)$$

where $K_{5/3}(x)$ is the modified Bessel function of the second kind, and $x = \nu/\nu_c$. The characteristic angular frequency $2\pi\nu_c$ is approximately 30 keV, as derived from estimates of the scattering timescale [60]. The derivation of Eq. (3.24) is based on classical electrodynamics assuming an instantaneous average radius of curvature of the positrons trajectories described by a gaussian distribution, which corresponds to the characteristic frequency ν_c . In reality, the positrons energy distribution is more complicated and a full quantum mechanical approach should also be considered. This is left for a future work, and in this paper we will assume that a single characteristic frequency ν_c is a valid approximation for our purpose. Nevertheless, it is important to keep in mind that the non-thermal spectrum calculation is less robust than the thermal emission spectrum outlined in Eq. (3.19).

Integrating over the modified Bessel function as specified in Eq. (3.24) provides a simple analytical approximation:¹⁴

¹³There are many parameters which enter our computations such as f or g . However, these parameters are not fundamental parameters of the system, and in principle could be computed from first principles. Such computations, however, are not feasible at this moment, as it requires good understanding of the strongly coupled QCD.

¹⁴It should be noted that the general form of the non-thermal spectrum can be expressed as:

$$F_\nu^{\text{non-th}} \propto x^\beta e^{-x}$$

where the Bremsstrahlung emission is dependent on the energy distribution of the positrons. Here, we adhere to the convention $\beta = 1/3$, as utilized in the original paper [60], which assumes that the positron beams are highly correlated.

$$x \int_x^\infty K_{5/3}(x') dx' \approx 1.81x^{1/3} e^{-x}. \quad (3.25)$$

This leads us to define a formula analogous to Eq. (3.21):

$$F_{\text{tot}}^{\text{non-th}} = \int_0^\infty d\nu F_\nu^{\text{non-th}}. \quad (3.26)$$

An expression for $F_\nu^{\text{non-th}}$ can be obtained with the following argument: the non-thermal radiation is emitted in a short pulse for a single collision event, but given the large number of collisions per unit of time within cosmologically large volumes, we can use Eq. (3.4) as an estimate of the average power emitted non-thermally. The average power, per AQN, is then simply given by:

$$\frac{dE_{\text{ann}}^{\text{non-th}}}{dt} = 4\pi R_{\text{AQN}}^2 F_{\text{tot}}^{\text{non-th}}, \quad (3.27)$$

where

$$F_\nu^{\text{non-th}} \approx \frac{2 \text{ GeV } f g}{4 \Gamma(4/3)} \frac{n_b \Delta v}{\nu_c} \left(\frac{R_{\text{eff}}}{R_{\text{AQN}}} \right)^2 \left(\frac{\nu}{\nu_c} \right)^{\frac{1}{3}} e^{-\nu/\nu_c}, \quad (3.28a)$$

and the spectral emissivity is:

$$\epsilon_\nu^{\text{non-th}} = 4\pi R^2 F_\nu^{\text{non-th}} n_{\text{AQN}}, \quad (3.28b)$$

where the Gamma function $\Gamma(4/3) \sim 0.893$. Additionally, Eq. (3.28a) can be recast as a function of T_{AQN} using Eq. (3.18):

$$F_\nu^{\text{non-th}} = \frac{16\alpha^{5/2}}{3\pi \Gamma(4/3)} \frac{g}{1-g} \frac{1}{\nu_c} \frac{T_{\text{AQN}}^{17/4}}{m_e^{1/4}} \left(\frac{\nu}{\nu_c} \right)^{\frac{1}{3}} e^{-\nu/\nu_c}. \quad (3.29)$$

Figure 3 shows the non-thermal X-ray spectral emissivity for various AQN temperatures, along with the thermal emission calculated in Section 3.2.5.

Note that, in addition to X-rays, other non-thermal electromagnetic radiations such as the direct production of 0.1-1 GeV gamma rays and a 511 keV line from electron-positron annihilation are possible, though less prominent [60, 65–67]. Our focus in this work is primarily on the dominant thermal and non-thermal emissions as derived above.

4 Simulations

In Section 3 we described the calculation of the spectral emissivity ϵ_ν^{th} and $\epsilon_\nu^{\text{non-th}}$ for the thermal and non-thermal processes, given the AQN number density n_{AQN} , baryon number density n_b and temperature T_{gas} and the average speed between dark matter and baryons Δv . The AQN specific intensity $I_\nu(\vec{\theta})$ at a given position $\vec{\theta}$ on the sky is given by the sum of the spectral emissivity along redshift for each line-of-sight in direction $\vec{\theta}$. Hydrodynamical simulations provide all the physical quantities needed as a function of 3D position in space \vec{r} , for different redshifts z , from which the sky projection can be performed.

The procedure is as follows: from the dark matter mass density, $\rho_{\text{DM}}(\vec{r}, z)$, we calculate the number density of AQNs, $n_{\text{AQN}}(\vec{r}, z)$. This is then combined with the baryons' number density, n_b , the gas temperature, T_{gas} , and the relative speed, Δv , to determine the AQN temperature, $T_{\text{AQN}}(\vec{r}, z)$. From there, the spectral emissivity, $\epsilon_\nu(\vec{r}, z)$, is calculated. A criteria to fix the ionization level of the baryonic matter also needs to be established. This section outlines the computation of $\epsilon_\nu(\vec{r}, z)$ and details the construction of the light-cone and the calculation of the specific intensity $I_\nu(\vec{\theta})$.

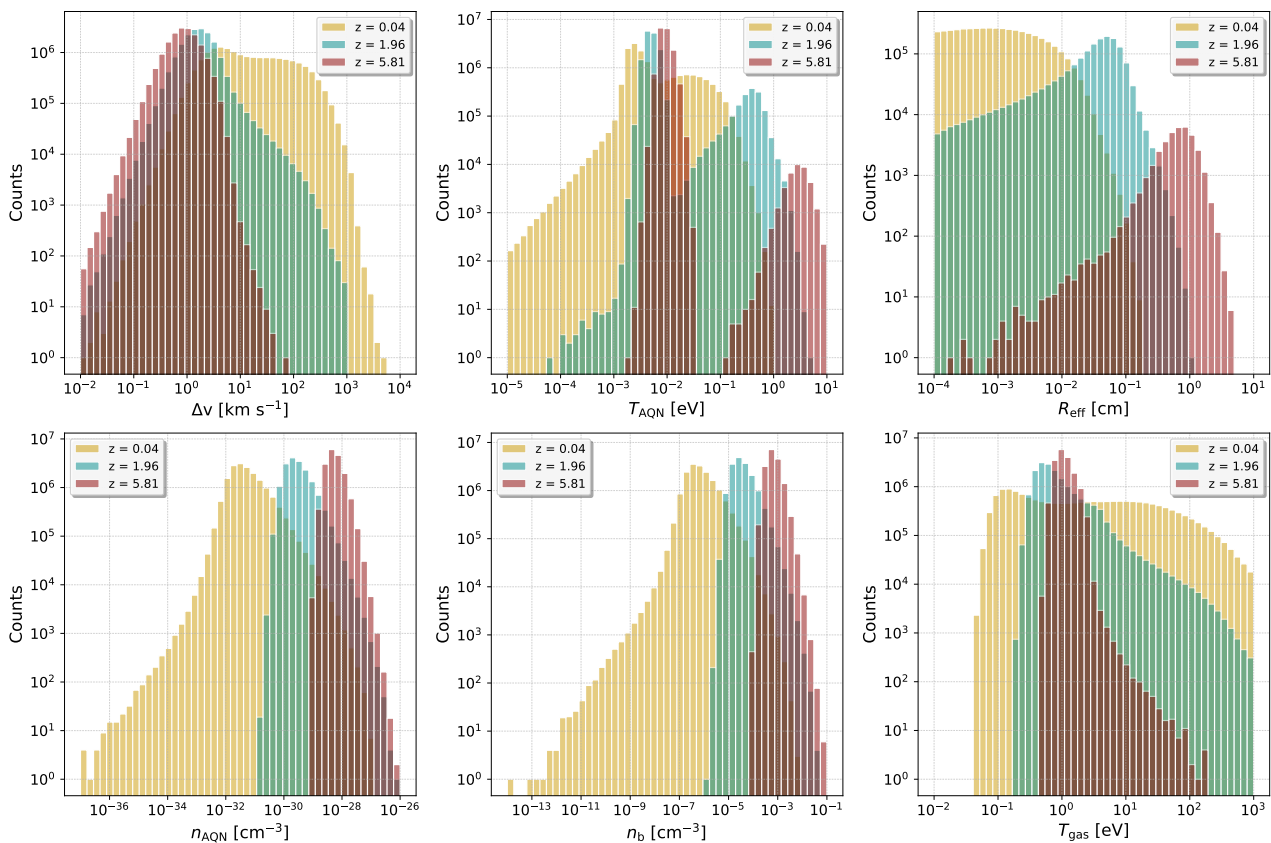


Figure 4. Histograms of the physical quantities relevant for the AQN emission for three different redshifts $z = [0.04, 1.96, 5.81]$. This is for an AQN mass of $m_{\text{AQN}} = 100$ g, which correspond to an AQN radius of $R_{\text{geo}} = 4.7 \times 10^{-5}$ cm. Other AQN masses are not display in order to avoid a confusing plot. We have assumed a mixed ionized case with an ionization temperature $T_{\text{gas}} = 2.6$ eV (3×10^4 K). From the top-left to the bottom-right panels: Δv is the relative speed between baryons and dark matter, T_{AQN} is the AQN electrosphere temperature, R_{eff} is the tail of the effective radius distribution (for most AQNs we have $R_{\text{eff}} = R_{\text{geo}}$), n_{AQN} is the number density of AQNs, n_b is the number density of baryons (assuming protons) and T_{gas} is the gas temperature.

4.1 Data cubes

We utilized the *Box3/hr* from the *Magneticum Pathfinder* suite of cosmological hydrodynamical simulations [68], which covers a comoving cosmological volume of $(128h^{-1}c \text{ Mpc})^3$ with 576^3 dark matter particles and an equal number of gas particles and periodic boundary conditions. The *Magneticum* simulations adopt the WMAP cosmology [69] with a Hubble constant of $H_0 = 70.4$ $\text{km s}^{-1} \text{ Mpc}^{-1}$, total matter density parameter $\Omega = 0.272$, a baryonic fraction of 16.8%, index of the primordial power spectrum $n = 0.963$, and normalization of the fluctuation amplitude $\sigma_8 = 0.809$. More information about the *Magneticum* project is available at www.magneticum.org.

The *Magneticum* simulations were conducted using the Tree/SPH code P-GADGET-3, an advancement of the publicly available P-GADGET-2 [70]. It incorporates an enhanced Smoothed Particle Hydrodynamics (SPH) solver [71] that includes improvements in numerical viscosity [72]. The simulations account for a range of physical processes such as metallicity-dependent gas cooling [73], star formation and stellar feedback [74, 75], UV background [76], chemical enrichment

[77, 78], and thermal conduction at 1/20th of the Spitzer level [79]. Additionally, the simulations monitor the evolution of supermassive black holes (SMBHs) and their associated feedback, building upon the foundational model by [74] with subsequent enhancements by [80] and [81]. The data cubes are 256^3 voxels and are given for eight time stamps which correspond to redshifts $z_i = [0, 0.252, 0.471, 1.18, 1.98, 2.792, 4.23, 5.34]$.

Since the key quantity for calculating the specific intensity $I_\nu(\vec{\theta})$ is the spectral emissivity $\epsilon_\nu(\vec{r}, z_i)$, we first compute ϵ_ν for the initial eight redshifts, and then construct the light-cone. The quantities directly obtained from the simulations are Δv , n_b , T_{gas} , and n_{AQN} (assuming a specific AQN mass for the latter). Conversely, the quantities derived from the simulations, T_{AQN} and R_{eff} , require knowledge of the baryon gas's ionization level, since the AQN signal is strongly dependent on the ionization level. The highest redshift of the simulation being $z = 5.34$, we know the Universe should be fully reionized, therefore the gas should be ionized in the entire light cone. In reality, the exact history of reionization and how it happens is still unknown, and moreover, as the Universe continues expanding and the galaxies and stars to form, there are regions where the gas cools down and returns to atomic form. How this is happening is still an active field of research. Therefore, as a conservative approach, we will consider three ionization levels in the following: 100% ionized, a mixed case where we assume that the gas below $T_{\text{gas}} = 2.6$ eV is in atomic form, and a fully neutral atomic case. Since it is expected that the Universe is in a highly ionized state, the fully neutral atomic case is not realistic, but we use it as a benchmark representing what the lowest AQN signal would be if the cross-section was only geometrical σ_{geo} .

Figure 4 shows the physical quantities relevant for the AQN emission for three different redshifts and for the mixed ionization case. The most interesting feature is the double structure histogram for T_{AQN} . This is coming from the gas temperature cut $T_{\text{gas}} = 2.6$ eV below which the baryons surrounding the AQNs are assumed in neutral atomic form. For the same baryon number density n_b and relative speed Δv , AQNs in a neutral atomic environment are cooler than the AQNs in a fully ionized environment by approximately two orders of magnitude. This separation is particularly strong at high redshift, but at lower redshift the double structure eventually merges in a single histogram with a bump in the middle, and at redshift $z = 0.04$, the average and dispersion of the T_{AQN} is mostly dominated by the AQN in the ionized environment. The top-right panel of Figure 4 shows that in the mixed ionized case, the majority of the AQNs have $R_{\text{eff}} = R_{\text{geo}}$ (the panel only shows the tail of the R_{eff} distribution, see the caption). We can use Figure 4 to anticipate what should happen in the fully ionized and fully neutral atomic cases (not shown): for the fully ionized case, only the high T_{AQN} histogram is populated, while in the fully neutral atomic case, only the low T_{AQN} histogram is populated. The impact on the observability of the AQN signal will be discussed later. In an ionized environment, all the AQNs have an effective radius $R_{\text{eff}} \gg R_{\text{geo}}$ at the highest redshift of our light-cone, but at lower redshift the distinction between the fully ionized and the mixed cases is not strong.

Figure 5 shows clearly the distinction between the neutral atomic environment ($T_{\text{gas}} < 2.6$ eV) and ionized environment ($T_{\text{gas}} > 2.6$ eV), and the sharp jump in T_{AQN} is what can also be seen in Figure 2 for various baryon number densities.

4.2 Calculation of the specific intensity I_ν

The calculation of $I_\nu(\vec{\theta})$ first requires the spectral emissivity $\epsilon_\nu(\vec{r}, z_i)$ within each cube, from which we subsequently construct the light cone. All the calculations are performed for three different average AQN masses $m_{\text{AQN}} = (10 \text{ g}, 100 \text{ g}, 1000 \text{ g})$, which correspond to an average radius $R_{\text{AQN}} = (1.9 \times 10^{-5} \text{ cm}, 4.1 \times 10^{-5} \text{ cm}, 8.8 \times 10^{-5} \text{ cm})$, and for the three ionization levels (fully ionized, mixed case and neutral atomic).

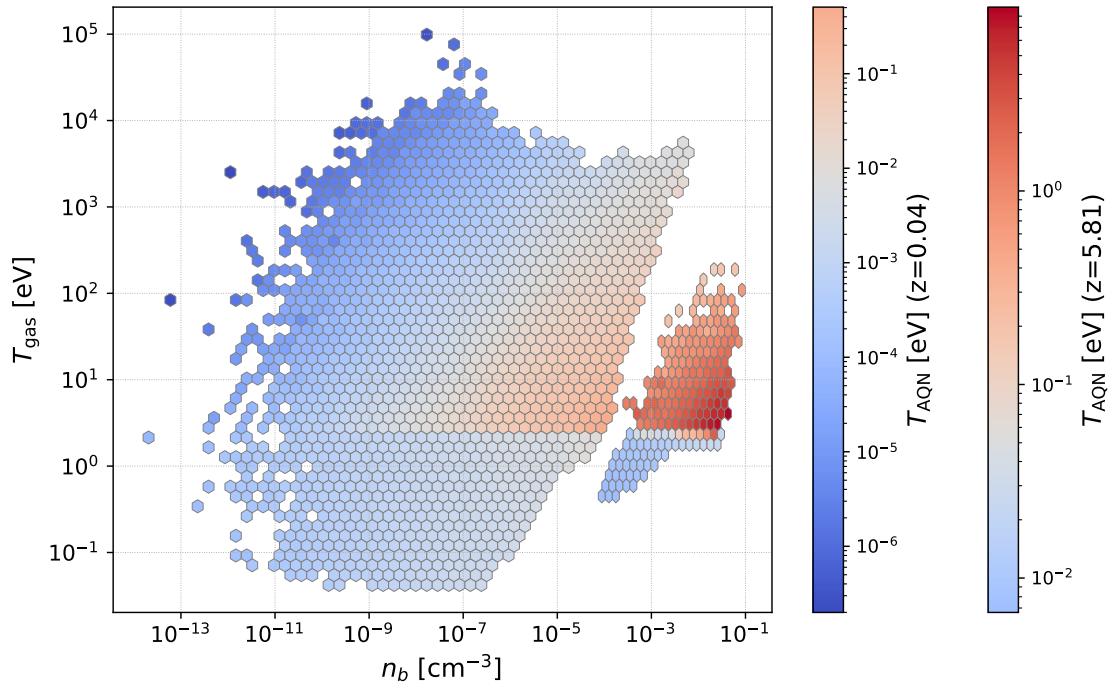


Figure 5. Average AQN temperature T_{AQN} as a function of the baryon number density n_b and the gas temperature T_{gas} for two different redshifts $z = [0.04, 5.81]$. The AQN physical properties are the same as in Figure 4.

It is more convenient to use comoving distances for the calculations, the corresponding quantities are labelled with the subscript C. The spectral emissivity $\epsilon_{\nu, \text{C}}(\vec{r}, z_i)$ at redshift z_i of the AQN-gas interaction, at comoving position \vec{r} is given by:

$$\epsilon_{\nu, \text{C}}(\vec{r}, z_i) = 4\pi R_{\text{AQN}}^2 F_{\nu}(T_{\text{AQN}}(\vec{r}, z_i)) n_{\text{AQN}, \text{C}}(\vec{r}, z_i) \quad (4.1)$$

where $n_{\text{AQN}, \text{C}}$ is the comoving AQN number density. $F_{\nu}(T_{\text{AQN}}(\vec{r}, z_i))$ is the emission spectrum, calculated using physical quantities at redshift z_i . $F_{\nu}(T_{\text{AQN}}(\vec{r}, z_i))$ is given by Eq. (3.19) or Eq. (3.28a) for the thermal or non-thermal process, respectively, or it can be the sum of both. The unit of $\epsilon_{\nu, \text{C}}$ is $\text{erg s}^{-1} \text{Hz}^{-1} \text{cm}^{-3}$. Note that F_{ν} and $n_{\text{AQN}, \text{C}}$ are calculated for each voxel \vec{r} of a data cube at redshift z_i . The AQN temperature $T_{\text{AQN}}(\vec{r}, z_i)$ is calculated using the procedure described in Section 3.2.4.

In order to calculate the specific intensity, $I_{\nu}(\vec{\theta})$, we must first construct a light cone of $\epsilon_{\nu, \text{C}}(\vec{r}, z)$ as a continuous function of redshift and where the large scale structures do not appear at the same position in the cubes as the redshift varies. The gaps between the sampled redshifts z_i are simply filled with copies of the nearest cube in comoving coordinates. For the redshift range $z = [0, 5.8]$, 49 cubes are needed. The cubes are adjacent to each other, do not overlap, and constitute the basis for our light cone. In order to eliminate the spatial correlation between cubes, we employ a technique commonly used in N-body simulation, which consists in randomly shifting and rotating each cube. The 49 adjacent data cubes are constructed from the original eight time stamps. We decided to not perform any interpolation between time stamps, and instead, for any redshift z_i , use the nearest time stamp as the data cube. This procedure results in a quantized distribution of average cosmological values, but it will not significantly affect our results. Figure 6 shows the cubes arrangements of the

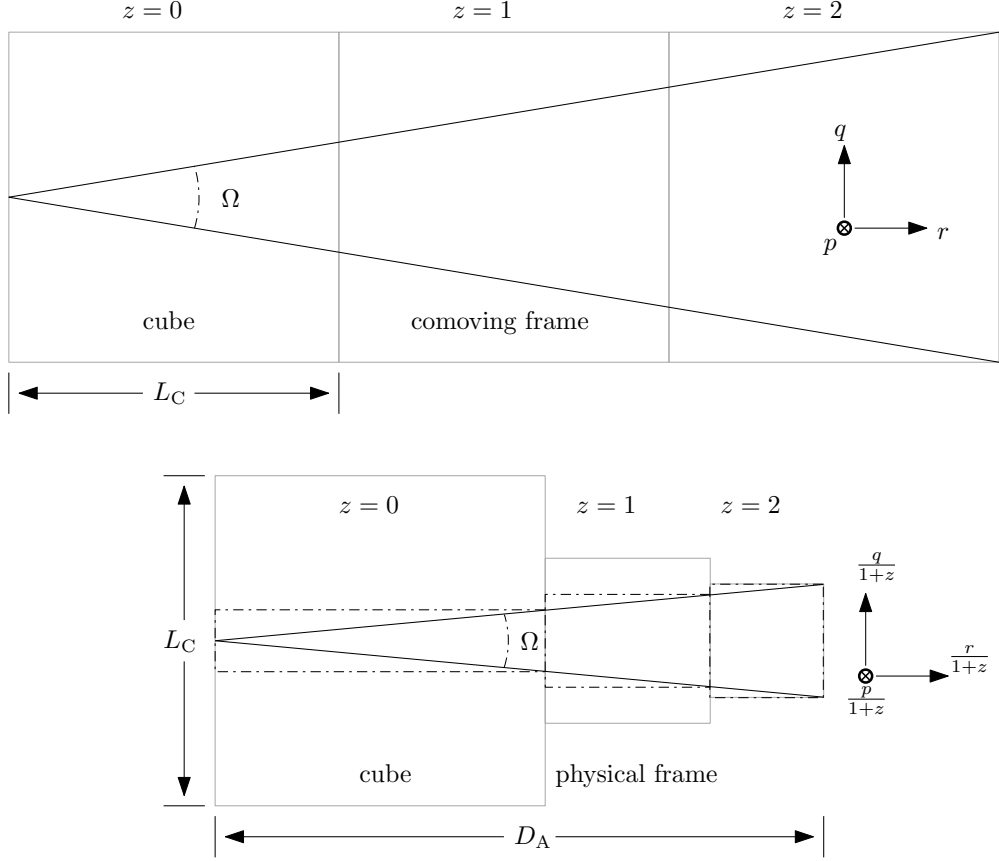


Figure 6. Illustrative construction of cubes in comoving (upper) and physical (lower) coordinates. (p, q, r) are the Cartesian comoving coordinates with r extending along the redshift axis. $D_A = (1+z)^{-2}D_L$ is the angular diameter distance. $L_C = 128h^{-1}\text{Mpc}$ is the comoving size of a cube. In a continuous space, the observer has the same solid angle Ω both in the comoving and physical frames. In the simulation, the space is divided into a series of subsequent cubes at discrete redshifts. The projection within each cube along Ω becomes parallel (dash-dotted), instead of conical (solid).

light cone from which the sky projection is later constructed, and a comparison between the physical and comoving frames.

Along a given line-of-sight $\vec{\theta}$ subtends a solid angle $d\Omega$, and the comoving volume element $dV_C = (1+z)^3 dV$ is given by:

$$dV_C = (1+z)^3 \frac{dp}{1+z} \frac{dq}{1+z} \frac{dr}{1+z} \approx (1+z)^3 d\Omega D_A^2(z) \frac{dr}{1+z}, \quad (4.2)$$

where $\vec{r} = (p, q, r)$ are Cartesian comoving coordinates¹⁵ with r along the redshift axis, and $D_A(z)$ is the angular diameter distance at redshift z . The comoving volume can be rewritten as:

$$dV_C \approx \frac{D_L^2(z)}{(1+z)^2} d\Omega dr, \quad (4.3)$$

¹⁵The use of Cartesian coordinates is justified by the small angle approximation, and (p, q, r) are expressed in physical units.

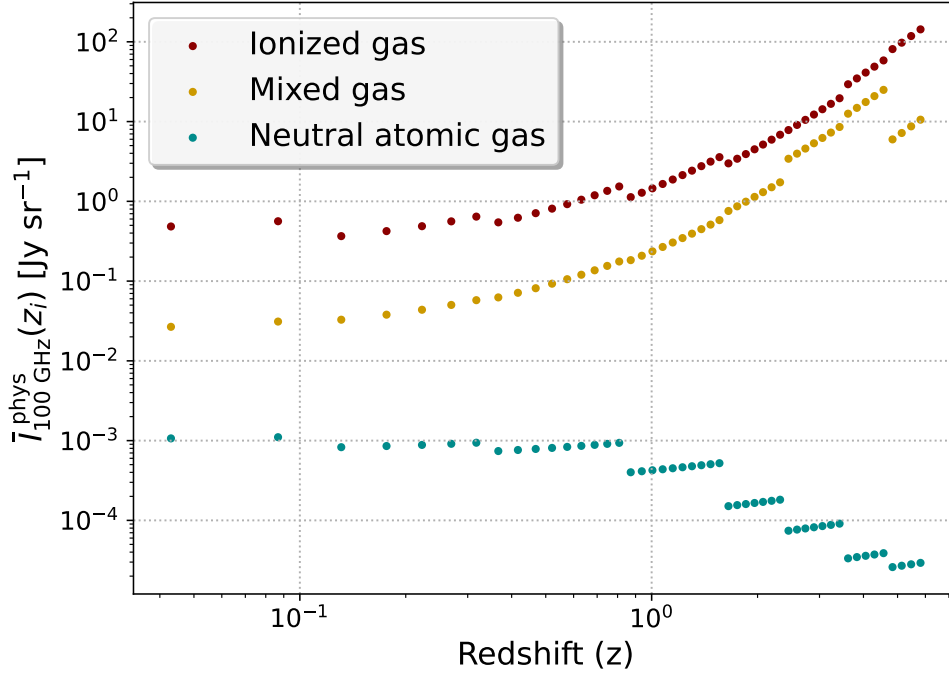


Figure 7. Average intensity $\bar{I}_{100 \text{ GHz}}^{\text{phys}}(z_i)$ as a function of redshift z_i (see Eq. 4.12) for an AQN mass $m_{\text{AQN}} = 10 \text{ g}$. Each dot indicates the average intensity in the data cube at particular redshift z_i . This plot shows which redshift contributes the most to the observed intensity depending on the ionization level of the environment (ionized, mixed or neutral atomic). The origin of the successive jumps in redshift is explained in the text: between two jumps, the same time stamp was used to generate the data cubes.

where $D_L(z) = (1+z)^2 D_A(z)$ is the luminosity distance at redshift z . Using Eq. (4.1), we define the $dL_{\nu'}(\vec{r}, z)$ the spectral luminosity [$\text{erg s}^{-1} \text{ Hz}^{-1}$] at rest-frame frequency $\nu' = (1+z)\nu$ emitted by a voxel (the source) at location (\vec{r}, z) and observed within the solid angle $d\Omega$:

$$dL_{\nu'}(\vec{r}, z) = \epsilon_{\nu', C}(\vec{r}, z) dV_C, \quad (4.4)$$

and the rest frame luminosity of the source [erg s^{-1}] in the physical frame is $dL_{\nu'}(\vec{r}, z) d\nu'$. The specific intensity, measured at frequency ν within $d\nu$ and solid angle $d\Omega$, can be expressed as:

$$\frac{\partial I_\nu(\vec{r}, z)}{\partial r} d\nu d\Omega dr = \frac{dL_{\nu'}(\vec{r}, z) d\nu'}{4\pi D_L^2(z)} = \frac{\epsilon_{\nu', C}(\vec{r}, z) d\nu' d\Omega}{4\pi D_L^2(z) (1+z)^2} dr. \quad (4.5)$$

We conclude that I_ν [$\text{erg s}^{-1} \text{ cm}^{-2} \text{ Hz}^{-1} \text{ sr}^{-1}$] is given by:

$$\begin{aligned} I_\nu(p, q) &= \int \frac{\partial I_\nu(\vec{r}, z)}{\partial r} dr \\ &= R_{\text{AQN}}^2 \int dr \frac{D_L^2(z)}{(1+z)^2} n_{\text{AQN}, C}(\vec{r}, z) \frac{F_{\nu'}(\vec{r}, z)}{D_L^2(z)} \cdot (1+z) \\ &= R_{\text{AQN}}^2 \int \frac{dr}{1+z} n_{\text{AQN}, C}(\vec{r}, z) F_{\nu'}(\vec{r}, z), \end{aligned} \quad (4.6)$$

Note that r is implicitly a function of z , but we keep z as an explicit variable as a marker of which data cube time stamp should be used (this is important when rewriting the integral in the discretized form). For analytical calculations, one may express r as a function of z , but for this work we are concerned with discretized 3-dimensional quantities. As shown in Figure 6, we have a stack of cubes with the same comoving size. Each cube contains discrete pixels of numerical values in Cartesian coordinates $\vec{r}_i = (p_i, q_i, r_i)$ at discrete redshift z_i . Then, for each cube at redshift z_i , the corresponding $I_\nu(p_i, q_i, z_i)$ is:

$$I_\nu(z_i, p_i, q_i) = \frac{R^2 \delta r}{1 + z_i} \sum_{r_i} n_{\text{AQN}, C}(p_i, q_i, r_i) F_{\nu'}(z_i, p_i, q_i, r_i), \quad (4.7)$$

where δr is the comoving lattice spacing between two nearby pixels in the r -direction. As shown in figure 6, projections of $I_\nu(p_i, q_i, z_i)$ in each cube are parallel, instead of conical, for simplicity in simulations. For each plate $I_\nu(p_i, q_i, z_i)$, only one square slice of size $\Delta p \times \Delta q$ contributes to the overall projection of intensity background. The Δp and Δq are redshift-dependent with the following relation:

$$\begin{aligned} \Delta p(z_i) = \Delta q(z_i) &= (1 + z_i) D_A(z_i) \cdot \theta, \\ \theta &= \frac{L_C}{(1 + z_{\text{max}}) D_A(z_{\text{max}})}, \end{aligned} \quad (4.8)$$

where $D_A(z_i) = (1 + z_i)^{-2} D_L(z_i)$ is the angular diameter distance, $\theta = \sqrt{\Omega}$ is the angle of the conical projection (see figure 6), L_C is the comoving size of a cube, z_{max} is the maximal redshift in the cubes. The range of (p_i, q_i) for a cube at redshift z_i is chosen to be:¹⁶

$$p_i \in [0, \Delta p(z_i)], \quad q_i \in [0, \Delta q(z_i)]. \quad (4.9)$$

Beyond this range, the data points are out of the projection light cone Ω and have no impact on the intensity function I_ν . The intensity spectrum $I_\nu(p_i, q_i, z_i)$ in the comoving frame can be converted to the physical frame:

$$I_\nu^{\text{phys}}(z_i, x_i, y_i) \equiv I_\nu(z_i, \frac{\Delta p(z_i)}{\Delta p(z_{\text{min}})} x_i, \frac{\Delta q(z_i)}{\Delta q(z_{\text{min}})} y_i), \quad (4.10)$$

where (x, y) is defined to be the physical Cartesian coordinate measured at redshift $z = z_{\text{min}}$ (the minimal nonzero z_i in the cubes):

$$(x_i, y_i) = \frac{1}{1 + z} (p_i, q_i) \Big|_{z=z_{\text{min}}} \quad (4.11)$$

such that the observation angle $\vec{\theta}$ can be specified by (x_i, y_i) . The total background intensity $I_{\text{tot}, \nu}^{\text{phys}}(x_i, y_i)$ is obtained by stacking up all $I_\nu^{\text{phys}}(z_i, x_i, y_i)$ plates:

$$I_{\text{tot}, \nu}^{\text{phys}}(x_i, y_i) = \sum_{z_i} I_\nu^{\text{phys}}(z_i, x_i, y_i). \quad (4.12)$$

Figure 7 shows the scaling of the AQN signal $\bar{I}_{100 \text{ GHz}}^{\text{phys}}(z_i)$ with redshift z_i for the three ionization levels of the environment, at $\nu = 100 \text{ GHz}$ and $m_{\text{AQN}} = 10 \text{ g}$. At high redshift, the matter (baryons

¹⁶Here we implicitly choose the projection plate (p_i, q_i) locating at one corner of the $p - q$ face of the cube, instead of locating near the center of the $p - q$ face. The choice of location is unimportant because the pixels will be randomized by shifting and rotating in each cube, as discussed earlier in this subsection.

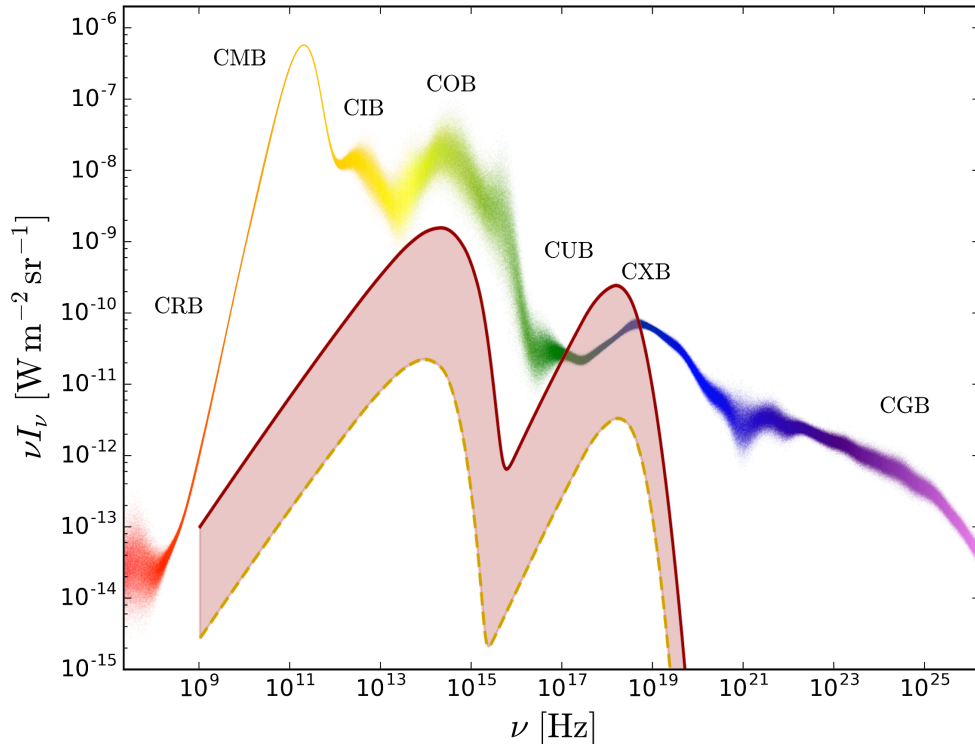


Figure 8. The colored scattered points represent the overall estimate of the continuous cosmic background, consistent with observations. This is Figure 9 from [82]. The light red region corresponds to the AQN global emission, delimited by a maximum (top red solid line) and a minimum (bottom yellow dashed line) corresponding to ($m_{\text{AQN}} = 100$ g, fully ionized) and ($m_{\text{AQN}} = 10$ g, mixed). The neutral atomic case is not shown here, but would have a spectral shape similar to the red solid line, although five orders of magnitude smaller.

and dark matter) number density is high, but the baryon temperature is generally not (see Figure 4). Therefore, it is not possible to intuitively predict whether the AQNs will generally be warmer (more emission) or colder (less emission). Figure 7 demonstrates that the decisive factor is primarily the ionization level of the environment: for a given redshift, i.e., with fixed number densities and baryon temperature, a more ionized environment leads to a higher AQN temperature and thus more AQN emission. The mixed environment shows a decrease in the emission at redshifts greater than $z \sim 5$. This is caused by the fact that the average baryon temperature decreases with redshift, and given our crude assumption of $T_{\text{cut}} = 2.6$ eV that separates ionized from neutral atomic states, the highest redshift cube turns out to be less ionized than all others. This decrease in intensity is also visible in Figure 5 as a decrease of the AQN temperature for $T_{\text{gas}} < 2.6$ eV. Additionally, Figure 7 indicates that in an ionized environment, large redshifts $z \gtrsim 2 - 3$ are the dominant contributors to the intensity measured at $z = 0$. This implies that when searching for the AQN signature using cross-correlations, the use of high-redshift tracers would be our best chance.

5 Results

The AQN emission will generate a monopole signal (i.e. global intensity) and anisotropies (i.e. intensity fluctuations). Both will be computed using the light-cone simulations. In the following, the

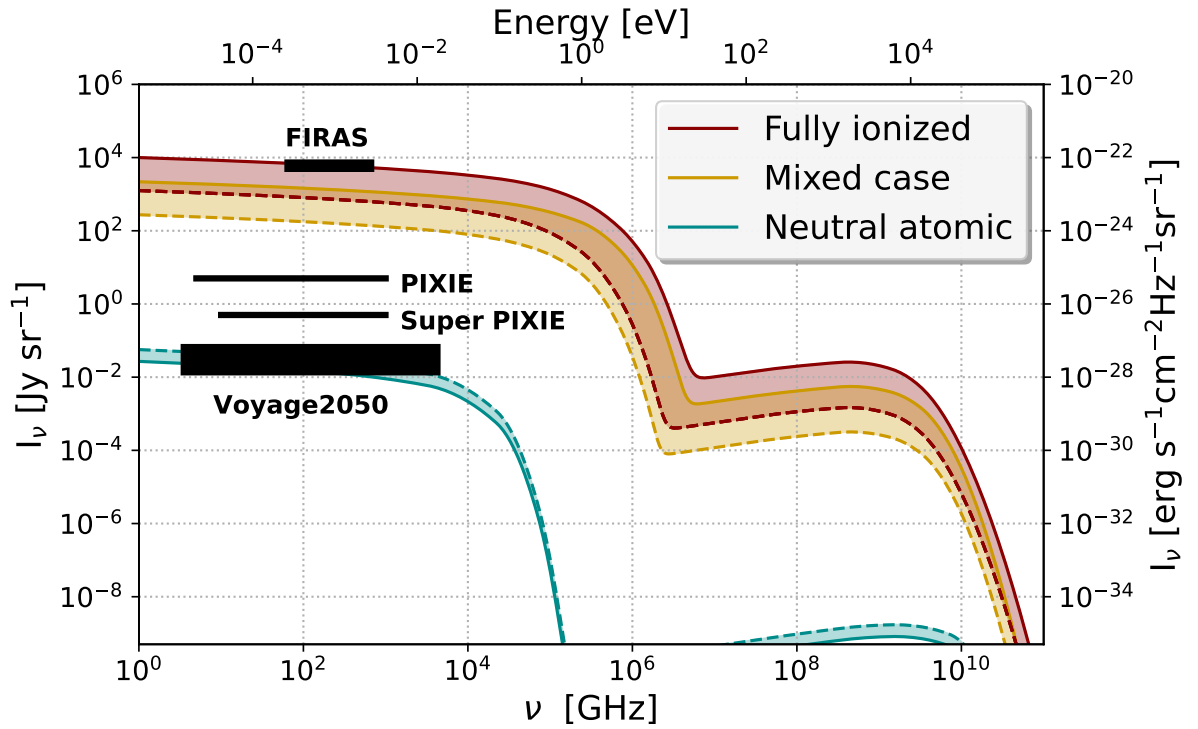


Figure 9. Global intensity I_ν of the AQN signal for the three ionization cases and two AQN masses $m_{\text{AQN}} = 10$ g (dashed line) and $m_{\text{AQN}} = 100$ g (solid line). The FIRAS rectangle is the current precision of the CMB frequency spectrum. The black rectangles represent the sensitivity range of proposed experiments (references can be found in the text).

calculations are performed using a combination of three AQN masses $m_{\text{AQN}} = [10, 100, 1000]$ g for three different environments: fully ionized, mixed and fully neutral atomic. The intensity of the AQN signal can vary by several orders of magnitude for the different mass/environment configurations. A most optimistic (maximum signal) and minimal configuration (minimal signal) will be identified below.

5.1 Monopole

The first step is to estimate the global AQN signal and compare it to the observed sky brightness as a function of frequency. In a recent review paper [82], the average sky brightness observations across all wavelengths were compiled, from radio to γ -ray, which is precisely what the AQN signal prediction should be compared to. Figure 9 from [82] was copied in Figure 8 and overlaid with the AQN global intensity calculated from the previous sections. The AQN signal is presented as a region delimited by a maximum (top red solid line) and a minimum (bottom yellow dashed line) corresponding to ($m_{\text{AQN}} = 100$ g, fully ionized) and ($m_{\text{AQN}} = 10$ g, mixed). The neutral atomic case is not shown because the line would be four orders of magnitude below the yellow dashed line, and it is known to not correspond to the real Universe. The maximum signal (top red solid line on Figure 8) and the neutral atomic case respectively define our most optimistic and minimum configurations. The light red region on Figure 8 highlights what we believe is the most realistic range for the AQN model¹⁷.

¹⁷Other combinations of AQN mass and environment will be discussed later.

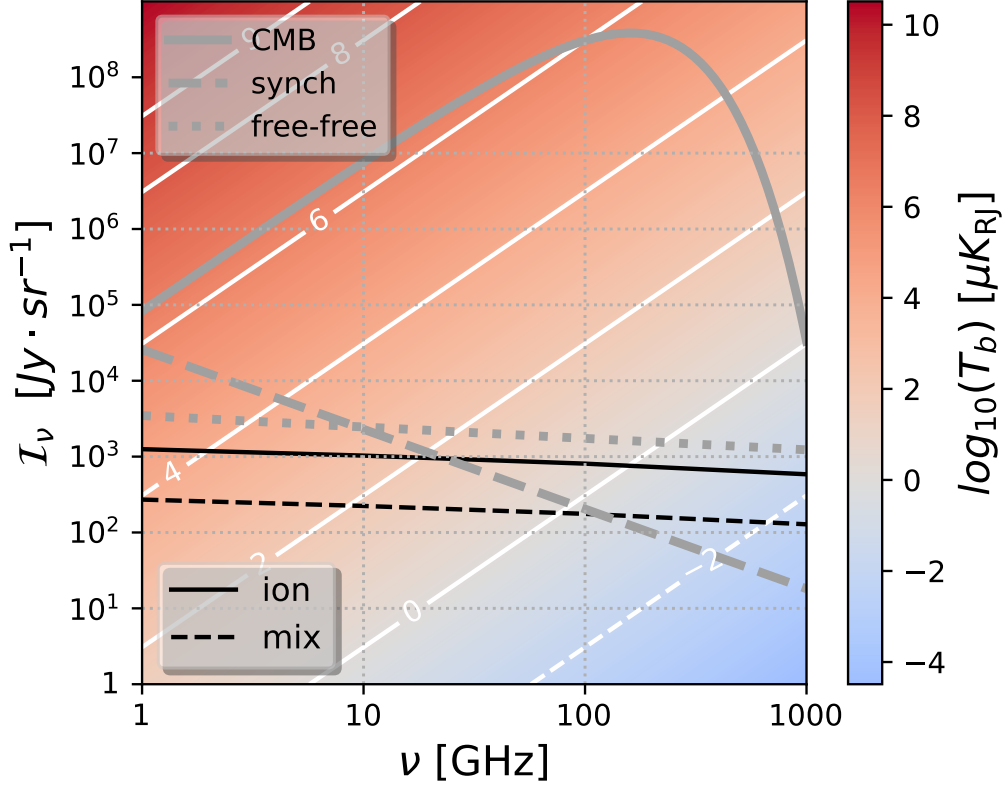


Figure 10. Brightness temperature in μK assuming the Rayleigh-Jeans regime for a given intensity I_ν (white solid lines) and frequency ν . The thick grey lines show the global specific intensity of the cosmic microwave background at $T_{\text{CMB}} = 2.725 \text{ K}$ (grey solid), synchrotron (grey dashed) and free-free (grey dotted) emissions. The black lines show the AQN emission for a mass $m_{\text{AQN}} = 10 \text{ g}$ and two different ionized environments, fully ionized and mixed (solid and dashed black lines respectively).

The two peaks at $\sim 10^{14} \text{ Hz}$ and $\sim 10^{18} \text{ Hz}$ correspond to the thermal and non-thermal emissions (see Figure 3). Overall, the AQN signal is, up to a few orders of magnitude, below the measured sky brightness, but as we will see later, possibly within the detection limit of recently operational instruments and upcoming observatories. On Figure 8, the maximum non-thermal emission exceeds the measured sky brightness in the soft X-ray regime, however, this should not be interpreted as ruling out the AQN model, for the following reasons: 1) depending on the AQN mass and the environment ionization, the non-thermal signal can be several orders of magnitude smaller; 2) As discussed in Section 3.3, the calculations of the non-thermal emission are based on the oversimplified assumption that all positrons emit Bremsstrahlung with the same cut-off frequency ν_c [60]. In reality, positrons have a broad velocity distribution, resulting in a broader spectrum than in Figure 8, but this is left for future work. Figure 9 shows the thermal and non-thermal signals together for the three ionization environments and the mass range $m_{\text{AQN}} = [10 - 100] \text{ g}$. In the ionized environment, the signal increases with m_{AQN} , while it decreases in a neutral atomic environment. The latter is expected because the ratio AQN area over volume scales as R_{AQN}^{-1} , meaning that for fixed total dark matter, more massive AQNs emit less radiation on average. On the other hand, in an ionized environment, this effect is compensated, and in fact reversed, by the increase of the effective radius. Consequently,

in an ionized environment, the absence of an AQN signal detection will set an upper bound constraint on m_{AQN} , while in a neutral atomic environment it will set a lower bound. The current detection limit of FIRAS, and of a few proposed experiments to measure the global intensity of the microwave sky, are shown on Figure 9. Within, what is likely, the most realistic range for m_{AQN} , and for a mixed or fully ionized environment, the AQN signal is not dramatically below the FIRAS detection limit. Experiments such as PIXIE [83], PRISM [84, 85], superPIXIE [86], and Voyage2050 [87] would have no problem detecting it. Interestingly, the sensitivity of Voyage2050 would even be capable of detecting the AQN signature in the most unlikely situation of a neutral atomic environment. The thermal emission (described in Section 3.2) which is strong in the radio, up to the optical frequencies, is build on much more theoretically solid computational scheme than the X-ray emission. For this reason, in the rest of this work, we will focus on the thermal emission.

Figure 10 shows the AQN thermal emission in the frequency range where the cosmic microwave background dominates the cosmological signal. The synchrotron and free-free foregrounds are shown as indicators of where the AQN model predictions stand. The Galactic dust and the Cosmic Infrared Background are not shown; they scale as $\sim \nu^2$, cross the primary CMB signal at $\nu \sim 800$ GHz and are $\sim 10^4$ Jy/sr at $\nu = 100$ GHz. Other sources of spectral distortion, such as the μ and y distortions, are shown on Figure 5 of [86]. Although the most optimistic AQN scenario is only marginally below the dominant foregrounds, the AQN signal of the minimal configuration (neutral atomic case) is comparable to the recombination signal of the CMB at $\sim 10^{-2} - 10^{-1}$ Jy/sr, which is the ultimate target of proposed spectral distortion experiments. At first approximation, the AQN signal could be confused with a free-free spectrum, but the slope is slightly different and future work will have to demonstrate if they can be disentangled, in particular with components separation techniques combined with cross-correlations.

5.2 Anisotropies

Intensity anisotropies is another prediction of the AQN model. Figure 11 shows the intensity anisotropies in the radio sky ($\nu \lesssim 1000$ GHz) for the three different ionization environments at $\nu = 100$ GHz. The neutral atomic environment (right panel) shows large structures at low redshift, since the low redshift universe dominates the signal, as was already seen in Figure 7. In the fully ionized case (left panel), it is the opposite, high redshift structures dominate and therefore exhibits very small structures, with a much larger intensity, also in agreement with Figure 7. The histograms show that the r.m.s. of the anisotropies have the same order of magnitude as the average of the signal itself, regardless of the ionization environment. This is potentially worrying since the primary CMB anisotropies are $\sim 10^5$ smaller than the CMB monopole intensity, which would make them comparable to the AQN signal. Fortunately, Figure 11 shows that when the intensity of the AQN radio anisotropies is high (ionized environment), the fluctuations take place at small angular scale, while when the anisotropy signal is low (neutral atomic environment), the fluctuations occur at relatively large angular scale (degree scale).

One can use the AQN signal maps from Figure 11 to calculate the angular power spectrum C_ℓ^{AQN} ¹⁸ to compare it to the known radio sky anisotropies. Figure 12 shows that for the fully ionized case, the high amplitude of anisotropies occur at high $\ell \sim 10^4$ ¹⁹, where the fluctuations of the primary CMB fluctuations are vanishing small and the signal is dominated by secondary anisotropies. Therefore, we can assert that the high amplitude of the AQN radio anisotropies do not conflict with the observed CMB anisotropy spectrum. The fully neutral atomic case is not shown, it peaks at $\ell \sim 200 - 400$ with much lower amplitude than the primary CMB (as expected from the right panel of Figure 11).

¹⁸This is done using the NaMaster package available from <https://namaster.readthedocs.io/en/latest/> [88]

¹⁹this is the limit of the Nbody simulation

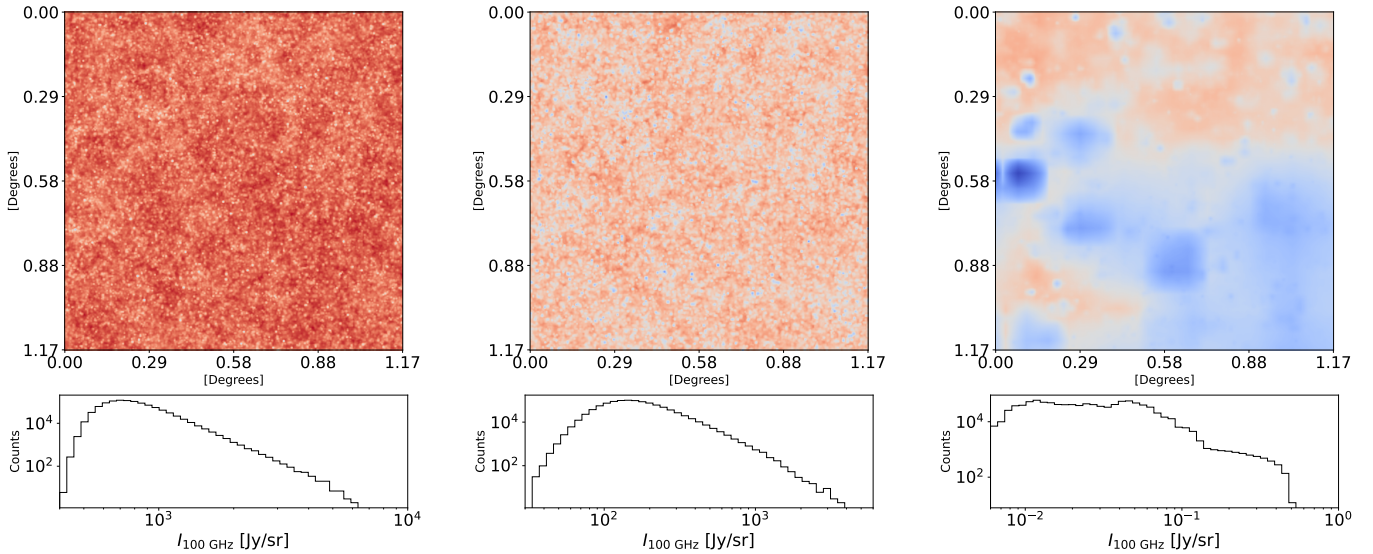


Figure 11. Specific intensity $I_\nu(\vec{\theta})$ at $\nu = 100$ GHz in units of Jy/sr for the three different environments, ionized, mix and neutral atomic for left, middle, right panels respectively. The top row shows the full light-cone 1.17×1.17 sq. deg. and the bottom row shows the histogram of $I_\nu(\vec{\theta})$.

How significantly are the AQN anisotropy contributing to the foreground secondary anisotropies? At $\ell \gtrsim 10^3$, the secondary anisotropies dominate the radio sky. For frequencies of interest in this work, $\nu \gtrsim 100$ GHz, the two main contributors of the extragalactic foregrounds are the thermal Sunyaev-Zeldovich and the Cosmic Infrared Background. The black dashed line on Figure 12 shows the South Pole Telescope signal for the 95 GHz channel [89], dominated by these foregrounds above $\ell \gtrsim 3000$. The AQN signal could be a contributor to the extragalactic foreground, but with an amplitude strongly dependent on m_{AQN} . If one assumes the delta function distribution for the AQN masses (as described in Sect. 2.3) then figure 12 naively suggests that high AQN mass ($m_{\text{AQN}} \gtrsim 10^2$ g) is apparently ruled out. However, any realistic mass distribution, e.g. a power law, is likely to decrease the intensity of the emission, which warrants a more careful and precise analysis of this region in future.

Since the AQN signal decreases as ν^{-2} , it is expected that the extragalactic CIB becomes dominant at higher frequency $\nu > 100$ GHz. The best frequency-scale window to look for the AQN anisotropy signal is $\ell \gtrsim 4000$ and $\nu \lesssim 100$ GHz, although this is also where the synchrotron foregrounds are dominant. One should also keep in mind that the AQN anisotropy signal exists for the entire frequency spectrum displayed in Figure 9. The detectability of the anisotropies in the infrared/optical spectrum is discussed in the section 6.2.

6 Discussion

In this paper, we have explored the electromagnetic signatures of the AQN dark matter model at cosmological scales. The AQN framework, initially motivated by the similar values of the baryon and dark matter mass density parameters, originates from the standard model of particle physics and incorporates the QCD axion as a solution to the strong $C\mathcal{P}$ problem. Conventional dark matter models usually assume the existence of a new dark sector weakly or very weakly interacting with normal matter. AQNs, on the other hand, interact strongly with normal matter without violating the canons

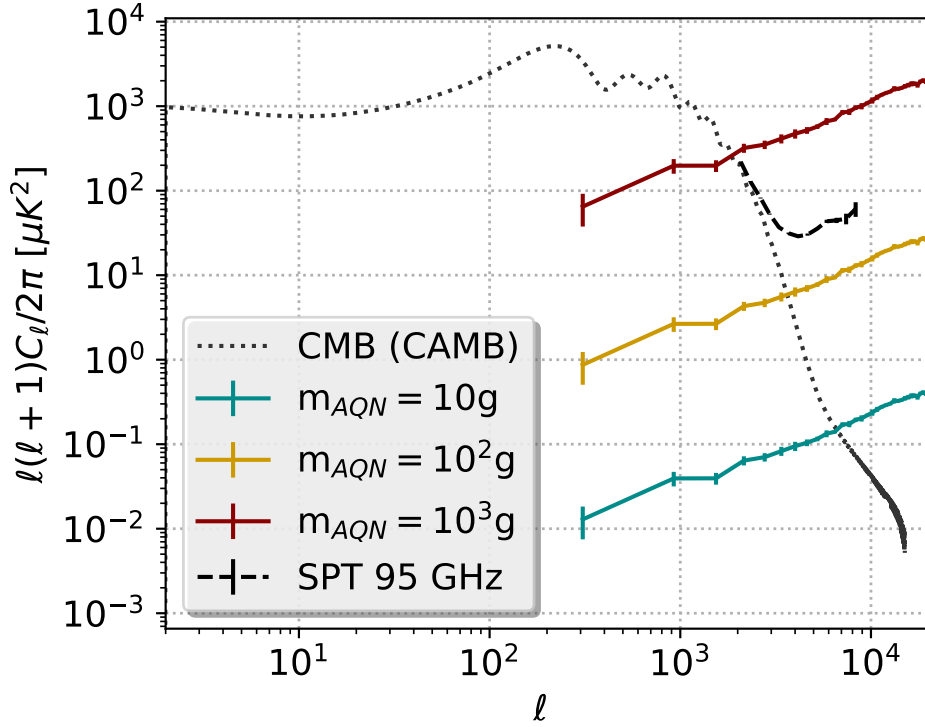


Figure 12. Anisotropy angular power spectrum for the CMB from the South Pole Telescope experiment at 95 GHz (dashed line, from [89]), compared to the theoretical spectrum using CAMB (dotted line). The colored solid lines show the AQN anisotropy signal at $\nu = 95$ GHz for different AQN masses in a fully ionized environment.

of the Big-Bang cosmology. Moreover, this exotic model may offer a solution to several outstanding cosmological problems.

6.1 Key results

1- The thermal radiation is dominated by Bremsstrahlung and is determined by the electrosphere temperature T_{AQN} . The main factor determining T_{AQN} , and therefore the amplitude of the emission, is the ionization fraction of the baryonic environment, higher ionization leading to higher emission. The underlying physical mechanism is that AQNs with $T_{\text{AQN}} \neq 0$ carry a small electrical charge, hence the Coulomb cross-section could significantly increase in an ionized environment.

2- The global intensity (monopole) is a signal which will modify the frequency spectrum of the combined synchrotron and free-free foregrounds. This is particularly relevant in the radio regime $\nu < 1000$ GHz, where the primary CMB and the foreground monopoles are strong. The amplitude is a function of the AQN mass m_{AQN} and of the ionization level of the environment. Higher m_{AQN} leads to higher amplitude, therefore current measurement could provide an upper bound for the AQN mass. A realistic average AQN mass predicts an amplitude one to two orders of magnitude below the current FIRAS limits.

3- For a given frequency, the AQN anisotropy amplitude has an intensity comparable to the global signal. The reason is that the AQN signal originates from the low redshift universe, where mass density fluctuations are strongly non-linear. The angular power spectrum analysis of the anisotropies

at $\nu = 100$ GHz showed that the C_ℓ peaks at high $\ell \sim 10^4$ with a high amplitude in a fully ionized environment and much lower $\ell \sim 10^2$ with a low amplitude in a fully neutral atomic environment. The AQN C_ℓ is not in conflict with measurements: the high amplitude case occurs at very small angular scale where the AQN signal is much smaller than extragalactic foregrounds (thermal Sunyaev-Zeldovich and Cosmic Infrared Background) and the low amplitude case at large scale is much smaller than the primary CMB.

4- The non-thermal radiation, which can extend up to a few dozens of keV, is caused by the positrons emitting Bremsstrahlung at the point of impact. It is based on simplified assumptions, which tend to overestimate the intensity of the signal at the characteristic frequency ν_c . Therefore, our prediction using the light-cone simulation should be taken with caution in the X-ray regime, although the predicted AQN energy spectrum monopole is within the range of the current observational limits.

6.2 Future work towards a possible detection

The light cone simulation reveals several interesting features which can help to design a target search for the AQN signal. The detection of the global signal and anisotropies requires distinct strategies.

1- Figures 8 and 9 show that the AQN thermal emission extends up to optical wavelength. It is the frequency range $\nu = [10^{13} - 10^{15}]$ Hz, where the intensity is the closest to the measured sky background, that the chance of a direct detection is highest. Table 2 shows the expected surface brightness I_ν calculated from the monopole AQN intensity for the maximum ($m_{\text{AQN}} = 100$ g and fully ionized) and minimum $m_{\text{AQN}} = 10$ g for the mixed ionized environment) cases shown in Figure 8. We emphasize that, since the monopole and the anisotropies have similar intensity, they also have similar surface brightness, therefore the monopole I_ν is a good estimate, to first approximation, of the anisotropy δI_ν .

Due to the Zodiacal light, the monopole is very difficult to measure in the infrared/optical. There are reports of Extragalactic Background Light excess across the infrared and optical spectrum (see the Figure 8 in [90] and references therein). Using the New Horizons-LORRI data, the Cosmic Optical Background appears to be brighter than expected [91, 92] and it is debated whether it could be linked to dark matter [93, 94]. However, constraints on AQN in the infrared/optical are most likely to first come from anisotropies. Anisotropy measurements already exist [95], and very low surface brightness fluctuations, such as shown in Table 2, are in principle achievable with the new generation of space based telescopes, Euclid [96] and the James Webb Space Telescope. This is left for future work, but ultimately, the consistency between the monopole and the anisotropy signals would constitute a strong test in the infrared/optical range (e.g. [94, 97]).

ν [Hz]	λ [μm]	$I_\nu _{\text{max,min}}$ [$m_{\text{AB}}/\text{arcsec}^2$]
10^{13}	30	26.7, 30.7
10^{14}	3	27.6, 32.1
3×10^{14}	1.0	28.7, 33.8
4.3×10^{14}	0.7	29.3, 35.1
10^{15}	0.3	31.2, 39.0

Table 2. Monopole surface brightness of the AQN signal in the infrared and optical range. $I_\nu|_{\text{max}}$ and $I_\nu|_{\text{min}}$ are taken from the light red region of Figure 8 for the corresponding frequencies.

2- Another interesting path of investigation is suggested by Figure 12: the South Pole Telescope will be reanalysed with the AQN signal amplitude parametrized as a function of ℓ and ν . This should give a strong upper bound on the AQN mass m_{AQN} . Extending this analysis to much lower frequency,

1 GHz $\lesssim \nu \lesssim$ 100 GHz, would be particularly interesting, since the AQN emission amplitude should scale as $\sim \nu^{-2}$ due to the near Bremsstrahlung-like spectral energy distribution. The Very Large Array Sky Survey, which is operating at 2 – 4 GHz with a nominal sensitivity of 69 μ Jy, seems to be particularly well suited [98]. Figure 10 also suggests another interesting test, by letting the AQN mass vary and using components separation to extract the primary CMB and the foreground signals.

3- Figure 7 shows that most of the global and fluctuation signals is coming from redshift $z > 1-2$. A direct AQN signal search, such as proposed in the previous two paragraphs could be improved if we cross-correlate data sets with a chosen redshift range overlap, such that the resulting signal-to-noise is improved while reducing contaminating sources, e.g. for sources at $z < 1$. A proof of concept that cross-correlations can boost the sensitivity and target a specific population was performed in [99]. By cross-correlating Herschel-SPIRE imaging and the Canada-France Imaging Survey (CFIS) Low Surface Brightness data ²⁰, it was shown that an r.m.s. surface brightness of $r_{AB} \sim 32.5$ mag/arcsec² is achievable statistically. According to Table 2, this would be in the range of interest.

4- Another approach consists in looking for the AQN signature in specific environments. In this work we focused on large scale structures, but the physical parameters characterizing the baryonic environment, such as gas temperature, ionization level and baryon density, are greatly dependent on the system. The AQN signature in radio, optical, UV and X-ray is being investigated in clusters of galaxies [100] and the Milky Way [101]. A different environment is not necessarily a specific object. For instance, we are investigating the effect of AQN energy injection in the pre-recombination era of the CMB, specifically how the μ and y spectral distortions and the optical depth are changed [102].

6.3 Future work: theory

A particularly interesting regime where AQN physics could be relevant is during the Dark Ages and the Cosmic Dawn. Although the Universe is in atomic form at the $\sim 99.9\%$ level during the dark ages, the number density of matter scales as $(1+z)^3$, significantly increasing the annihilation rate. The resulting energy injection between recombination and reionization will precede the formation of the first stars, changing the number density of free electrons and, consequently, the optical depth. Constraints on energy injection during the dark ages already exist for decaying and annihilating dark matter models, primarily through the optical depth measured from Planck [1, 103]. AQNs can also alter the history of recombination. The challenge with these calculations is that, unlike dark matter decay and annihilation models, the injected photons cover a large energy range, including the resonant Ly α line. Therefore, proper inclusion of AQN physics in recombination and dark ages studies must account for atomic physics, not just the injected energy.

As the universe approaches cosmic dawn, a 21 cm line signal can develop, which the AQN physics can also impact. It is known that whether the 21 cm line is in emission or absorption at a given redshift z depends on the temperature of the surrounding radiation $T_\gamma(z)$, the matter temperature $T_{\text{gas}}(z)$, and the color temperature of the Ly α photons $T_\alpha(z)$. It is usually assumed that T_γ is the CMB temperature at z , but if dark matter is made of AQNs, the impact on 21 cm line could be altered in two opposite ways: injected photons will provide an additional source of photons in the radio background, strengthening the 21 cm absorption, but high-energy photons will reheat the matter, reducing 21 cm absorption. The effect is similar to a decaying or annihilating dark matter [104], but with the AQN dark matter a full atomic treatment is necessary.

The significant source of radio photons from AQN-baryon interaction can also have a cosmological consequence at low frequency. Below $\nu < 1 - 10$ GHz, an excess of radiation relative to the CMB, once the known foregrounds have been removed, has been known since the 80s, known as the

²⁰products from the Ultraviolet Near-Infrared Optical Northern Survey (UNIONS)

ARCADE excess [105]. Its origin, whether extragalactic or within the Milky Way, is still debated. The extrapolation of the AQN signal well below ~ 1 GHz in Figure 8 could be such a source, but at these frequencies, it is necessary to consider the physics of AQNs up to very high redshifts, possibly recombination, which requires significant theoretical development.

6.4 Concluding remarks

The key element of the AQN construction is that the DM and visible components are described as two different phases of the same fundamental QCD theory of the Standard Model. This model predicts the injection of energy to surrounding space at all redshifts and in very broad frequency bands, as we have shown in this work. The AQN signal is proportional to the dark and visible components, i.e. $\propto \rho_{\text{DM}} \cdot n_{\text{b}}$ ²¹, but we have also shown that purely ordinary matter parameters such as the gas temperature and the ionization rate strongly impact the dark matter signature. Therefore, the state of the baryonic environment plays a crucial role in the intensity of the dark matter signal. This is the most dramatic difference between canonical DM models to the AQN framework because dark matter and baryonic matter are strongly and non-trivially entangled. This property may dramatically modify many features during the long evolution of the Universe. The model is consistent with all presently available cosmological, astrophysical, satellite and ground-based observations and may even shed some light on a number of long-standing puzzles and mysteries as mentioned in the text. Without anticipating on the possible success or failure of the AQN model, it definitely offers an exciting and refreshing approach to the problem of the nature of dark matter, considering that the WIMP paradigm, despite a dramatic improvement of instrumentation over the past 40 years, still has not found any sign of dark matter.

Acknowledgments

FM, XL, LVW, AZ and MS acknowledges the support from NSERC. We thank Gary Hinshaw, Kirit Karkare and Ryley Hill for useful discussions. KD acknowledges support by the COMPLEX project from the European Research Council (ERC) under the European Union’s Horizon 2020 research and innovation program grant agreement ERC-2019-AdG 882679 as well as by the Deutsche Forschungsgemeinschaft (DFG, German Research Foundation) under Germany’s Excellence Strategy - EXC-2094 - 390783311.

The calculations for the hydrodynamical simulations were carried out at the Leibniz Supercomputer Center (LRZ) under the project pr83li.

The data in this paper were analyzed with open-source python packages `numpy` [106], `scipy` [107], `astropy` [108], `matplotlib` [109], and `NaMaster` [88].

A Natural and C.G.S. units conversion

The natural unit expressions given in this paper are convenient in order to grasp the orders of magnitude of the different phenomena using well known particle physics quantities, however, a conversion to physical units is necessary in order to do the calculations. In this Appendix, we provide the recipe to convert various expressions between different unit system. Table 3 shows how to convert between C.G.S and natural unit for most quantities used in this work. Note that, with natural unit, any physical quantity has the dimension of energy, where the dimension could be any integer \mathbb{Z} . Energy is conveniently expressed in electron-volts, although Table 3 shows the unit conversion from/to natural

²¹as opposed to $\propto \rho_{\text{DM}}$ for decaying dark matter and ρ_{DM}^2 for annihilating dark matter

units using the erg unit for energy. In order to avoid any confusion, we should ideally indicate which units are used for a particular quantity, for instance, using Table 3 and $1 \text{ eV} = 1.6021766 \times 10^{-12} \text{ erg}$, a length ℓ in C.G.S, natural (erg) and natural (eV) units would be given by:

$$\ell_{\text{CGS}} = \ell_{\text{Nat,erg}^{-1}} (\hbar c)_{\text{CGS}} = \ell_{\text{Nat,GeV}^{-1}} \frac{(\hbar c)_{\text{CGS}}}{0.0016021766} \quad (\text{A.1})$$

Implying that $1 \text{ GeV}^{-1} = 1.9732698 \times 10^{-14} \text{ cm}$. Using the same reasoning, a time t would be given by:

$$t_{\text{CGS}} = t_{\text{Nat,erg}^{-1}} \hbar_{\text{CGS}} = t_{\text{Nat,GeV}^{-1}} \frac{\hbar_{\text{CGS}}}{0.0016021766} \quad (\text{A.2})$$

implying that $1 \text{ GeV}^{-1} = 6.5821196 \times 10^{-25} \text{ s}$. However, the choice of a particular unit system is generally not indicated, meaning that, when converting a particular quantity (e.g. flux) from natural to C.G.S, it is necessary to know that we are dealing with a flux (in $\text{erg s}^{-1} \text{ cm}^{-2}$).

Table 3. Conversion table between C.G.S and natural units for most quantities used in this work, where the latter are expressed in erg, the unit of energy in C.G.S..

Quantity	C.G.S	Natural [erg]
Length ℓ	[cm]	$[\text{erg}^{-1}] = \frac{[\text{cm}]}{\hbar c}$
Time t	[s]	$[\text{erg}^{-1}] = \frac{[\text{s}]}{\hbar}$
Mass m	[g]	$[\text{erg}] = [\text{g}]c^2$
Velocity v	$[\text{cm s}^{-1}]$	$[1] = [\text{cm s}^{-1}] \frac{1}{c}$
Momentum p	$[\text{g cm s}^{-1}]$	$[\text{erg}] = [\text{g cm s}^{-1}]c$
Cross-section σ	$[\text{cm}^2]$	$[\text{erg}^{-2}] = \frac{[\text{cm}^2]}{(\hbar c)^2}$
Collision rate Γ	$[\text{s}^{-1}]$	$[\text{erg}] = [\text{s}^{-1}]\hbar$
Frequency ν	[Hz]	$[\text{erg}] = [\text{Hz}]\hbar$
Angular frequency $2\pi\nu$	[rad Hz]	$[\text{erg}] = [\text{rad Hz}]\hbar$
Temperature T	[K]	$[\text{erg}] = [\text{K}]k_B$

References

- [1] Planck Collaboration, N. Aghanim, Y. Akrami, M. Ashdown, J. Aumont, C. Baccigalupi et al., *Planck 2018 results. VI. Cosmological parameters*, *Astronomy & Astrophysics* **641** (2020) A6 [[1807.06209](#)].
- [2] G. Bertone and T.M.P. Tait, *A new era in the search for dark matter*, *Nature* **562** (2018) 51 [[1810.01668](#)].
- [3] R.N. Mohapatra and V.L. Teplitz, *Primordial nucleosynthesis constraint on massive, stable, strongly interacting particles*, *Phys. Rev. Lett.* **81** (1998) 3079 [[hep-ph/9804420](#)].
- [4] R.H. Cyburt, B.D. Fields, V. Pavlidou and B.D. Wandelt, *Constraining strong baryon dark matter interactions with primordial nucleosynthesis and cosmic rays*, *Phys. Rev. D* **65** (2002) 123503 [[astro-ph/0203240](#)].

Table 4. The equations referenced in the left column are written in natural and C.G.S units for completeness and to ease the numerical calculations.

Eq.(#)	Natural	C.G.S
(3.5)	$\frac{16}{3}T_{\text{AQN}}^4 \frac{\alpha^{5/2}}{\pi} \left(\frac{T_{\text{AQN}}}{m_e}\right)^{1/4}$	$\frac{16\alpha^{5/2}k_B^4 T_{\text{AQN}}^4}{3\pi\hbar^3 c^2} \sqrt[4]{\frac{k_B T_{\text{AQN}}}{m_e c^2}}$
(3.7)	$\frac{4\pi R^2}{\sqrt{2\pi\alpha}} (m_e T_{\text{AQN}}) \left(\frac{T_{\text{AQN}}}{m_e}\right)^{1/4}$	$\frac{4\pi R^2 k_B m_e T_{\text{AQN}}}{\sqrt{2\pi\alpha\hbar^2}} \left(\frac{k_B T_{\text{AQN}}}{m_e c^2}\right)^{1/4}$
(3.11)	$8\alpha m_e^2 R_{\text{AQN}}^2 \left(\frac{T_{\text{AQN}}}{T_{\text{gas}}}\right)^2 \sqrt{\frac{T_{\text{AQN}}}{m_e}}$	$8\alpha \left(\frac{m_e c R_{\text{AQN}}}{\hbar}\right)^2 \left(\frac{T_{\text{AQN}}}{T_{\text{gas}}}\right)^2 \sqrt{\frac{k_B T_{\text{AQN}}}{m_e c^2}}$
(3.15)	$m_e \left[\frac{2\text{GeV}}{8\alpha^{3/2} T_{\text{gas}}^2} f(1-g) 3\pi n_b \Delta v R_{\text{AQN}}^2 \right]^{4/7}$	$\frac{m_e c^2}{k_B} \left[\frac{3\pi}{8} \frac{2\text{GeV}}{\alpha^{3/2} k_B^2} \frac{f(1-g) R_{\text{AQN}}^2 \Delta v n_b}{T_{\text{gas}}^2} \right]^{4/7}$
(3.17)	$m_e^{1/17} \left[\frac{3\pi}{4} \frac{2\text{GeV}}{16\alpha^{5/2}} f(1-g) \Delta v n_b \right]^{4/17}$	$\frac{1}{k_B} \left[\frac{3\pi}{64} \frac{2\text{GeV}}{\alpha^{5/2}} \frac{\hbar^3 c^{5/2}}{f(1-g) m_e^{1/4} n_b \Delta v} \right]^{4/17}$
(3.19)	$\frac{4}{45} \frac{T_{\text{AQN}}^3 \alpha^{5/2}}{\pi} \left(\frac{T_{\text{AQN}}}{m_e}\right)^{1/4} H \left(\frac{h\nu}{T_{\text{AQN}}}\right)$	$\frac{4\alpha^{5/2} k_B^3}{45\pi\hbar^2 c^2} T_{\text{AQN}}^3 \sqrt[4]{\frac{k_B T_{\text{AQN}}}{m_e c^2}} H \left(\frac{h\nu}{k_B T_{\text{AQN}}}\right)$
(3.29)	$\frac{16\alpha^{5/2}}{3\pi\Gamma(4/3)} \frac{g}{1-g} \frac{1}{v_c} \frac{T_{\text{AQN}}^{17/4}}{m_e^{1/4}} \left(\frac{v}{v_c}\right)^{1/3} e^{-v/v_c}$	$\frac{16\alpha^{5/2}}{3\pi\Gamma(4/3)} \frac{k_B^{17/4}}{\hbar^3 c^{5/2}} \frac{g}{1-g} \frac{1}{v_c} \frac{T_{\text{AQN}}^{17/4}}{m_e^{1/4}} \left(\frac{v}{v_c}\right)^{1/3} e^{-v/v_c}$

- [5] Y. Ali-Haïmoud, J. Chluba and M. Kamionkowski, *Constraints on Dark Matter Interactions with Standard Model Particles from Cosmic Microwave Background Spectral Distortions*, *Phys. Rev. Lett.* **115** (2015) 071304 [[1506.04745](#)].
- [6] Y. Ali-Haïmoud, *Testing dark matter interactions with CMB spectral distortions*, *Phys. Rev. D* **103** (2021) 043541 [[2101.04070](#)].
- [7] S.L. Dubovsky and D.S. Gorbunov, *Small second acoustic peak from interacting cold dark matter?*, *Phys. Rev. D* **64** (2001) 123503 [[astro-ph/0103122](#)].
- [8] X. Chen, S. Hannestad and R.J. Scherrer, *Cosmic microwave background and large scale structure limits on the interaction between dark matter and baryons*, *Phys. Rev. D* **65** (2002) 123515.
- [9] C. Dvorkin, K. Blum and M. Kamionkowski, *Constraining dark matter-baryon scattering with linear cosmology*, *Phys. Rev. D* **89** (2014) 023519 [[1311.2937](#)].
- [10] V. Gluscevic and K.K. Boddy, *Constraints on Scattering of keV–TeV Dark Matter with Protons in the Early Universe*, *Phys. Rev. Lett.* **121** (2018) 081301 [[1712.07133](#)].
- [11] K.K. Boddy and V. Gluscevic, *First Cosmological Constraint on the Effective Theory of Dark Matter-Proton Interactions*, *Phys. Rev. D* **98** (2018) 083510 [[1801.08609](#)].
- [12] K.K. Boddy, V. Gluscevic, V. Poulin, E.D. Kovetz, M. Kamionkowski and R. Barkana, *Critical assessment of CMB limits on dark matter-baryon scattering: New treatment of the relative bulk velocity*, *Phys. Rev. D* **98** (2018) 123506 [[1808.00001](#)].
- [13] W.L. Xu, C. Dvorkin and A. Chael, *Probing sub-GeV Dark Matter-Baryon Scattering with Cosmological Observables*, *Phys. Rev. D* **97** (2018) 103530 [[1802.06788](#)].
- [14] Z. Li, V. Gluscevic, K.K. Boddy and M.S. Madhavacheril, *Disentangling Dark Physics with Cosmic Microwave Background Experiments*, *Phys. Rev. D* **98** (2018) 123524 [[1806.10165](#)].
- [15] Z. Li et al., *The Atacama Cosmology Telescope: limits on dark matter-baryon interactions from DR4 power spectra*, *JCAP* **02** (2023) 046 [[2208.08985](#)].
- [16] H. Tashiro, K. Kadota and J. Silk, *Effects of dark matter-baryon scattering on redshifted 21 cm signals*, *Phys. Rev. D* **90** (2014) 083522 [[1408.2571](#)].
- [17] J.B. Muñoz, E.D. Kovetz and Y. Ali-Haïmoud, *Heating of Baryons due to Scattering with Dark Matter During the Dark Ages*, *Phys. Rev. D* **92** (2015) 083528 [[1509.00029](#)].

- [18] J.B. Muñoz and A. Loeb, *Constraints on Dark Matter-Baryon Scattering from the Temperature Evolution of the Intergalactic Medium*, *JCAP* **11** (2017) 043 [[1708.08923](#)].
- [19] K.K. Rogers, C. Dvorkin and H.V. Peiris, *Limits on the Light Dark Matter–Proton Cross Section from Cosmic Large-Scale Structure*, *Phys. Rev. Lett.* **128** (2022) 171301 [[2111.10386](#)].
- [20] E.O. Nadler, V. Gluscevic, K.K. Boddy and R.H. Wechsler, *Constraints on Dark Matter Microphysics from the Milky Way Satellite Population*, *Astrophys. J. Lett.* **878** (2019) 32 [[1904.10000](#)].
- [21] DES collaboration, *Milky Way Satellite Census. III. Constraints on Dark Matter Properties from Observations of Milky Way Satellite Galaxies*, *Phys. Rev. Lett.* **126** (2021) 091101 [[2008.00022](#)].
- [22] K. Maamari, V. Gluscevic, K.K. Boddy, E.O. Nadler and R.H. Wechsler, *Bounds on velocity-dependent dark matter-proton scattering from Milky Way satellite abundance*, *Astrophys. J. Lett.* **907** (2021) L46 [[2010.02936](#)].
- [23] R.S. Chivukula, A.G. Cohen, S. Dimopoulos and T.P. Walker, *Bounds on Halo Particle Interactions From Interstellar Calorimetry*, *Phys. Rev. Lett.* **65** (1990) 957.
- [24] A. Bhoonah, J. Bramante, F. Elahi and S. Schon, *Calorimetric Dark Matter Detection With Galactic Center Gas Clouds*, *Phys. Rev. Lett.* **121** (2018) 131101 [[1806.06857](#)].
- [25] D. Wadekar and G.R. Farrar, *Gas-rich dwarf galaxies as a new probe of dark matter interactions with ordinary matter*, *Phys. Rev. D* **103** (2021) 123028 [[1903.12190](#)].
- [26] A. Bhoonah, J. Bramante, S. Schon and N. Song, *Detecting composite dark matter with long-range and contact interactions in gas clouds*, *Phys. Rev. D* **103** (2021) 123026 [[2010.07240](#)].
- [27] B. Qin and X.-P. Wu, *Constraints on the interaction between dark matter and baryons from cooling flow clusters*, *Phys. Rev. Lett.* **87** (2001) 061301 [[astro-ph/0106458](#)].
- [28] L. Chuzhoy and A. Nusser, *Consequences of Short-Range Interactions between Dark Matter and Protons in Galaxy Clusters*, *APJ* **645** (2006) 950 [[astro-ph/0408184](#)].
- [29] J. Hu and Y.-Q. Lou, *Collisional interaction limits between dark matters and baryons in ‘cooling flow’ clusters*, *Mon. Not. Roy. Astron. Soc.* **384** (2008) 814 [[0711.3555](#)].
- [30] PANDAX collaboration, *Search for Light Dark Matter with Ionization Signals in the PandaX-4T Experiment*, *Phys. Rev. Lett.* **130** (2023) 261001 [[2212.10067](#)].
- [31] LZ collaboration, *First Dark Matter Search Results from the LUX-ZEPLIN (LZ) Experiment*, *Phys. Rev. Lett.* **131** (2023) 041002 [[2207.03764](#)].
- [32] XENON collaboration, *First Dark Matter Search with Nuclear Recoils from the XENONnT Experiment*, *Phys. Rev. Lett.* **131** (2023) 041003 [[2303.14729](#)].
- [33] T. Bringmann and M. Pospelov, *Novel direct detection constraints on light dark matter*, *Phys. Rev. Lett.* **122** (2019) 171801 [[1810.10543](#)].
- [34] J. Bramante, B.J. Kavanagh and N. Raj, *Scattering Searches for Dark Matter in Subhalos: Neutron Stars, Cosmic Rays, and Old Rocks*, *Phys. Rev. Lett.* **128** (2022) 231801 [[2109.04582](#)].
- [35] J. Bramante, J. Kumar, G. Mohlabeng, N. Raj and N. Song, *Light dark matter accumulating in planets: Nuclear scattering*, *Phys. Rev. D* **108** (2023) 063022 [[2210.01812](#)].
- [36] L. Di Luzio et al., *Probing the axion–nucleon coupling with the next generation of axion helioscopes*, *Eur. Phys. J. C* **82** (2022) 120 [[2111.06407](#)].
- [37] L. Di Luzio, M. Fedele, M. Giannotti, F. Mescia and E. Nardi, *Stellar evolution confronts axion models*, *JCAP* **02** (2022) 035 [[2109.10368](#)].
- [38] P. Carena, G. Co, M. Giannotti, A. Lella, G. Lucente, A. Mirizzi et al., *Cross section for supernova axion observation in neutrino water Čerenkov detectors*, *Phys. Rev. C* **109** (2024) 015501 [[2306.17055](#)].

- [39] K. Griest and M. Kamionkowski, *Unitarity limits on the mass and radius of dark-matter particles*, *Phys. Rev. Letters* **64** (1990) 615.
- [40] M. Cirelli, A. Strumia and J. Zupan, *Dark Matter*, **2406.01705**.
- [41] E. Witten, *Cosmic separation of phases*, *Phys. Rev. D* **30** (1984) 272.
- [42] E. Farhi and R.L. Jaffe, *Strange matter*, *Phys. Rev. D* **30** (1984) 2379.
- [43] A. de Rujula and S.L. Glashow, *Nuclearites-a novel form of cosmic radiation*, *Nature* **312** (1984) 734.
- [44] A.R. Zhitnitsky, ‘Nonbaryonic’ dark matter as baryonic colour superconductor, *JCAP* **10** (2003) 010 [[hep-ph/0202161](#)].
- [45] D.J.E. Marsh, *Axion cosmology*, *Physics Reports* **643** (2016) 1 [[1510.07633](#)].
- [46] A. Zhitnitsky, *Axion quark nuggets. Dark matter and matter-antimatter asymmetry: Theory, observations and future experiments*, *Modern Physics Letters A* **36** (2021) 2130017 [[2105.08719](#)].
- [47] X. Liang and A. Zhitnitsky, *Axion field and the quark nugget’s formation at the QCD phase transition*, *Phys. Rev. D* **94** (2016) 083502 [[1606.00435](#)].
- [48] S. Ge, X. Liang and A. Zhitnitsky, *Cosmological C P -odd axion field as the coherent Berry’s phase of the Universe*, *Phys. Rev. D* **96** (2017) 063514 [[1702.04354](#)].
- [49] S. Ge, X. Liang and A. Zhitnitsky, *Cosmological axion and a quark nugget dark matter model*, *Phys. Rev. D* **97** (2018) 043008 [[1711.06271](#)].
- [50] S. Ge, K. Lawson and A. Zhitnitsky, *The Axion Quark Nugget Dark Matter Model: Size Distribution and Survival Pattern*, *Phys. Rev. D* **99** (2019) 116017 [[1903.05090](#)].
- [51] M.G. Alford, A. Schmitt, K. Rajagopal and T. Schafer, *Color superconductivity in dense quark matter*, *Rev. Mod. Phys.* **80** (2008) 1455 [[0709.4635](#)].
- [52] N. Raza, L. Van Waerbeke and A. Zhitnitsky, *Solar Corona Heating by the Axion Quark Nugget Dark Matter*, *Phys. Rev. D* **98** (2018) 103527 [[1805.01897](#)].
- [53] K. Lawson, X. Liang, A. Mead, M.S.R. Siddiqui, L. Van Waerbeke and A. Zhitnitsky, *Gravitationally trapped axions on Earth*, *Phys. Rev. D* **100** (2019) 043531 [[1905.00022](#)].
- [54] P. Gorham, *Antiquark nuggets as dark matter: New constraints and detection prospects*, *Phys. Rev. D* **86** (2012) 123005 [[1208.3697](#)].
- [55] V.V. Flambaum and A.R. Zhitnitsky, *Primordial Lithium Puzzle and the Axion Quark Nugget Dark Matter Model*, *Phys. Rev. D* **99** (2019) 023517 [[1811.01965](#)].
- [56] A. Zhitnitsky, *Cold dark matter as compact composite objects*, *Phys. Rev. D* **74** (2006) 043515 [[astro-ph/0603064](#)].
- [57] K. Lawson and A.R. Zhitnitsky, *The 21cm Absorption Line and Axion Quark Nugget Dark Matter Model*, *Phys. Dark Univ.* **24** (2019) 100295 [[1804.07340](#)].
- [58] O.P. Santillán and A. Morano, *Neutrino emission and initial evolution of axionic quark nuggets*, *Phys. Rev. D* **104** (2021) 083530 [[2011.06747](#)].
- [59] J. Singh Sidhu, R.J. Scherrer and G. Starkman, *Antimatter as Macroscopic Dark Matter*, *Phys. Lett. B* **807** (2020) 135574 [[2006.01200](#)].
- [60] M.M. Forbes and A.R. Zhitnitsky, *Diffuse x-rays: Directly observing dark matter?*, *JCAP* **0801** (2008) 023 [[astro-ph/0611506](#)].
- [61] M.M. Forbes and A.R. Zhitnitsky, *WMAP Haze: Directly Observing Dark Matter?*, *Phys. Rev. D* **78** (2008) 083505 [[0802.3830](#)].
- [62] M.M. Forbes, K. Lawson and A.R. Zhitnitsky, *The Electrosphere of Macroscopic ‘Quark Nuclei’: A Source for Diffuse MeV Emissions from Dark Matter*, *Phys. Rev. D* **82** (2010) 083510 [[0910.4541](#)].

- [63] A. Zhitnitsky, *Structure formation paradigm and axion quark nugget dark matter model*, *Physics of the Dark Universe* **40** (2023) 101217 [[2302.00010](#)].
- [64] S. Ge, H. Rachmat, M.S.R. Siddiqui, L. Van Waerbeke and A. Zhitnitsky, *X-ray annual modulation observed by XMM-Newton and Axion Quark Nugget dark matter*, *Physics of the Dark Universe* **36** (2022) 101031 [[2004.00632](#)].
- [65] D.H. Oaknin and A.R. Zhitnitsky, *511-KeV photons from color superconducting dark matter*, *Phys. Rev. Lett.* **94** (2005) 101301 [[hep-ph/0406146](#)].
- [66] A. Zhitnitsky, *The Width of the 511-KeV Line from the Bulge of the Galaxy*, *Phys. Rev.* **D76** (2007) 103518 [[astro-ph/0607361](#)].
- [67] K. Lawson and A.R. Zhitnitsky, *Diffuse cosmic gamma-rays at 1-20 MeV: A trace of the dark matter?*, *JCAP* **0801** (2008) 022 [[0704.3064](#)].
- [68] K. Dolag, E. Komatsu and R. Sunyaev, *SZ effects in the Magneticum Pathfinder simulation: comparison with the Planck, SPT, and ACT results*, *Mon. Not. R. Astron. Soc.* **463** (2016) 1797 [[1509.05134](#)].
- [69] E. Komatsu, J. Dunkley, M.R.olta, C.L. Bennett, B. Gold, G. Hinshaw et al., *Five-Year Wilkinson Microwave Anisotropy Probe Observations: Cosmological Interpretation*, *Astrophys. J. Supp.* **180** (2009) 330 [[0803.0547](#)].
- [70] V. Springel, *The cosmological simulation code GADGET-2*, *Mon. Not. R. Astron. Soc.* **364** (2005) 1105 [[astro-ph/0505010](#)].
- [71] A.M. Beck, G. Murante, A. Arth, R.S. Remus, A.F. Teklu, J.M.F. Donnert et al., *An improved SPH scheme for cosmological simulations*, *Mon. Not. R. Astron. Soc.* **455** (2016) 2110 [[1502.07358](#)].
- [72] K. Dolag, F. Vazza, G. Brunetti and G. Tormen, *Turbulent gas motions in galaxy cluster simulations: the role of smoothed particle hydrodynamics viscosity*, *Mon. Not. R. Astron. Soc.* **364** (2005) 753 [[astro-ph/0507480](#)].
- [73] R.P.C. Wiersma, J. Schaye and B.D. Smith, *The effect of photoionization on the cooling rates of enriched, astrophysical plasmas*, *Mon. Not. R. Astron. Soc.* **393** (2009) 99 [[0807.3748](#)].
- [74] V. Springel, T. Di Matteo and L. Hernquist, *Modelling feedback from stars and black holes in galaxy mergers*, *Mon. Not. R. Astron. Soc.* **361** (2005) 776 [[astro-ph/0411108](#)].
- [75] V. Springel and L. Hernquist, *Cosmological smoothed particle hydrodynamics simulations: a hybrid multiphase model for star formation*, *Mon. Not. R. Astron. Soc.* **339** (2003) 289 [[astro-ph/0206393](#)].
- [76] F. Haardt and P. Madau, *Modelling the UV/X-ray cosmic background with CUBA*, in *Clusters of Galaxies and the High Redshift Universe Observed in X-rays*, D.M. Neumann and J.T.V. Tran, eds., p. 64, Jan., 2001 [[astro-ph/0106018](#)].
- [77] L. Tornatore, S. Borgani, K. Dolag and F. Matteucci, *Chemical enrichment of galaxy clusters from hydrodynamical simulations*, *Mon. Not. R. Astron. Soc.* **382** (2007) 1050 [[0705.1921](#)].
- [78] L. Tornatore, S. Borgani, F. Matteucci, S. Recchi and P. Tozzi, *Simulating the metal enrichment of the intracluster medium*, *Mon. Not. R. Astron. Soc.* **349** (2004) L19 [[astro-ph/0401576](#)].
- [79] A. Arth, K. Dolag, A.M. Beck, M. Petkova and H. Lesch, *Anisotropic thermal conduction in galaxy clusters with MHD in Gadget*, *arXiv e-prints* (2014) arXiv:1412.6533 [[1412.6533](#)].
- [80] D. Fabjan, S. Borgani, L. Tornatore, A. Saro, G. Murante and K. Dolag, *Simulating the effect of active galactic nuclei feedback on the metal enrichment of galaxy clusters*, *Mon. Not. R. Astron. Soc.* **401** (2010) 1670 [[0909.0664](#)].
- [81] M. Hirschmann, K. Dolag, A. Saro, L. Bachmann, S. Borgani and A. Burkert, *Cosmological simulations of black hole growth: AGN luminosities and downsizing*, *Mon. Not. R. Astron. Soc.* **442** (2014) 2304 [[1308.0333](#)].

- [82] R. Hill, K.W. Masui and D. Scott, *The Spectrum of the Universe*, *Applied Spectroscopy* **72** (2018) 663 [1802.03694].
- [83] A. Kogut, D.J. Fixsen, D.T. Chuss, J. Dotson, E. Dwek, M. Halpern et al., *The Primordial Inflation Explorer (PIXIE): a nulling polarimeter for cosmic microwave background observations*, *JCAP* **2011** (2011) 025 [1105.2044].
- [84] PRISM Collaboration, P. Andre, C. Baccigalupi, D. Barbosa, J. Bartlett, N. Bartolo et al., *PRISM (Polarized Radiation Imaging and Spectroscopy Mission): A White Paper on the Ultimate Polarimetric Spectro-Imaging of the Microwave and Far-Infrared Sky*, *arXiv e-prints* (2013) arXiv:1306.2259 [1306.2259].
- [85] P. André, C. Baccigalupi, A. Banday, D. Barbosa, B. Barreiro, J. Bartlett et al., *PRISM (Polarized Radiation Imaging and Spectroscopy Mission): an extended white paper*, *JCAP* **2014** (2014) 006 [1310.1554].
- [86] A. Kogut, M.H. Abitbol, J. Chluba, J. Delabrouille, D. Fixsen, J.C. Hill et al., *CMB Spectral Distortions: Status and Prospects*, in *Bulletin of the American Astronomical Society*, vol. 51, p. 113, Sept., 2019, DOI [1907.13195].
- [87] J. Chluba, M.H. Abitbol, N. Aghanim, Y. Ali-Haïmoud, M. Alvarez, K. Basu et al., *New horizons in cosmology with spectral distortions of the cosmic microwave background*, *Experimental Astronomy* **51** (2021) 1515 [1909.01593].
- [88] D. Alonso, J. Sanchez, A. Slosar and LSST Dark Energy Science Collaboration, *A unified pseudo- C_ℓ framework*, *Mon. Not. R. Astron. Soc.* **484** (2019) 4127 [1809.09603].
- [89] C.L. Reichardt, L. Shaw, O. Zahn, K.A. Aird, B.A. Benson, L.E. Bleem et al., *A Measurement of Secondary Cosmic Microwave Background Anisotropies with Two Years of South Pole Telescope Observations*, *APJ* **755** (2012) 70 [1111.0932].
- [90] K. Mattila and P. Väisänen, *Extragalactic background light: inventory of light throughout the cosmic history*, *Contemporary Physics* **60** (2019) 23 [1905.08825].
- [91] T.R. Lauer, M. Postman, J.R. Spencer, H.A. Weaver, S.A. Stern, G.R. Gladstone et al., *Anomalous Flux in the Cosmic Optical Background Detected with New Horizons Observations*, *APJL* **927** (2022) L8 [2202.04273].
- [92] T. Symons, M. Zemcov, A. Cooray, C. Lisse and A.R. Poppe, *A Measurement of the Cosmic Optical Background and Diffuse Galactic Light Scaling from the $R < 50$ au New Horizons-LORRI Data*, *APJ* **945** (2023) 45 [2212.07449].
- [93] J.L. Bernal, G. Sato-Polito and M. Kamionkowski, *Cosmic Optical Background Excess, Dark Matter, and Line-Intensity Mapping*, *Phys. Rev. Letters* **129** (2022) 231301 [2203.11236].
- [94] K. Nakayama and W. Yin, *Anisotropic cosmic optical background bound for decaying dark matter in light of the LORRI anomaly*, *Phys. Rev. D* **106** (2022) 103505 [2205.01079].
- [95] K. Mitchell-Wynne, A. Cooray, Y. Gong, M. Ashby, T. Dolch, H. Ferguson et al., *Ultraviolet luminosity density of the universe during the epoch of reionization*, *Nature Communications* **6** (2015) 7945 [1509.02935].
- [96] J.C. Cuillandre, E. Bertin, M. Bolzonella, H. Bouy, S. Gwyn, S. Isani et al., *Euclid: Early Release Observations – Programme overview and pipeline for compact- and diffuse-emission photometry*, *arXiv e-prints* (2024) arXiv:2405.13496 [2405.13496].
- [97] R. Hill, D. Scott, D.J. McLeod, R.J. McLure, S.C. Chapman and J.S. Dunlop, *An optimal ALMA image of the Hubble Ultra Deep Field in the era of JWST: obscured star formation and the cosmic far-infrared background*, *Mon. Not. R. Astron. Soc.* **528** (2024) 5019 [2309.10988].
- [98] M. Lacy, S.A. Baum, C.J. Chandler, S. Chatterjee, T.E. Clarke, S. Deustua et al., *The Karl G. Jansky Very Large Array Sky Survey (VLASS). Science Case and Survey Design*, *Publications of the Astronomical Society of the Pacific* **132** (2020) 035001 [1907.01981].

- [99] S. Lim, R. Hill, D. Scott, L. van Waerbeke, J.-C. Cuillandre, R.G. Carlberg et al., *Constraints on galaxy formation from the cosmic-far-infrared-background - optical-imaging cross-correlation using Herschel and UNIONS*, *Mon. Not. R. Astron. Soc.* **525** (2023) 1443 [[2203.16545](#)].
- [100] J. Sommer and et al., *The glow of axion quark nugget dark matter: (ii) galaxy clusters*, *In preparation* (2024) .
- [101] M. Sekatchev and et al., *Axion quark nuggets: A recipe for a glowing milky way?*, *In preparation* (2024) .
- [102] F. Majidi and et al., *Axion quark nuggets in the pre-recombination era*, *In preparation* (2024) .
- [103] D. Green, P.D. Meerburg and J. Meyers, *Aspects of dark matter annihilation in cosmology*, *JCAP* **2019** (2019) 025 [[1804.01055](#)].
- [104] K. Short, J.L. Bernal, A. Raccanelli, L. Verde and J. Chluba, *Enlightening the dark ages with dark matter*, *JCAP* **2020** (2020) 020 [[1912.07409](#)].
- [105] D.J. Fixsen, A. Kogut, S. Levin, M. Limon, P. Lubin, P. Mirel et al., *ARCADE 2 Measurement of the Absolute Sky Brightness at 3-90 GHz*, *APJ* **734** (2011) 5 [[0901.0555](#)].
- [106] C.R. Harris, K.J. Millman, S.J. van der Walt, R. Gommers, P. Virtanen, D. Cournapeau et al., *Array programming with NumPy*, *Nature* **585** (2020) 357 [[2006.10256](#)].
- [107] P. Virtanen, R. Gommers, T.E. Oliphant, M. Haberland, T. Reddy, D. Cournapeau et al., *SciPy 1.0: fundamental algorithms for scientific computing in Python*, *Nature Methods* **17** (2020) 261 [[1907.10121](#)].
- [108] Astropy Collaboration, A.M. Price-Whelan, B.M. Sipőcz, H.M. Günther, P.L. Lim, S.M. Crawford et al., *The Astropy Project: Building an Open-science Project and Status of the v2.0 Core Package*, *Astronomical Journal* **156** (2018) 123 [[1801.02634](#)].
- [109] J.D. Hunter, *Matplotlib: A 2D Graphics Environment*, *Computing in Science and Engineering* **9** (2007) 90.